HHS Public Access

Author manuscript

Cell Chem Biol. Author manuscript; available in PMC 2018 October 19.

Published in final edited form as:

Cell Chem Biol. 2017 October 19; 24(10): 1259–1275.e6. doi:10.1016/j.chembiol.2017.08.009.

Heme Binding Biguanides Target Cytochrome P450 Dependent Cancer Cell Mitochondria

Zhijun Guo[1], **Irina F. Sevrioukova**[2], **Ilia Denisov**[3], **Xia Zhang**[1], **Ting-Lan Chiu**[1], **Dafydd G. Thomas**[4], **Eric A. Hanse**[1], **Rebecca A. D. Cuellar**[1], **Yelena V. Grinkova**[3], **Vanessa Wankhede Langenfeld**[1], **Daniel S. Swedien**[1], **Justin D. Stamschror**[1], **Juan Alvarez**[1], **Fernando Luna**[1,5], **Adela Galván**[1,5], **Young Kyung Bae**[6], **Julia D. Wulfkuhle**[7], **Rosa I. Gallagher**[7], **Emanuel F. Petricoin 3rd**[7], **Beverly Norris**[1], **Craig M. Flory**[1], **Robert J. Schumacher**[1], **M. Gerard O'Sullivan**[1], **Qing Cao**[1], **Haitao Chu**[1], **John D. Lipscomb**[1], **William M. Atkins**[8], **Kalpna Gupta**[1], **Ameeta Kelekar**[1], **Ian A. Blair**[9], **Jorge H. Capdevila**[10], **John R. Falck**[11], **Stephen G. Sligar**[3], **Thomas L. Poulos**[2], **Gunda Georg**[1], **Elizabeth Ambrose**[1], and **David A. Potter**[1]

[1]Univ. of Minnesota, Minneapolis, MN

[2]University of California, Irvine, Irvine, CA

[3]University of Illinois Urbana-Champaign, Urbana, IL

[4]University of Michigan, Ann Arbor, MN

[5]Unidad de Investigacion Biomedica en Cancer, Instituto Nacional de Cancerologia-Instituto de Investigaciones Biomedicas, UNAM, Mexico

[6]Yeungnam University, Daegu, Korea

[7]George Mason University, Fairfax, VA

[8]University of Washington, Seattle, WA

[9]University of Pennsylvania, Philadelphia, PA

Corresponding Author and Lead Contact: David A. Potter, M.D., Ph.D.; dapotter@umn.edu, Department of Medicine HOT Division and Masonic Cancer Center, University of Minnesota.

Author Contributions:

Conception and design: D.A. Potter

Development of methodology: D.A. Potter, Z. Guo

Acquisition of data: Z. Guo, I.F. Sevrioukova, I. Denisov, W.M. Atkins, X. Zhang, T-L. Chiu, D.G. Thomas, E.A. Hanse, R. Cuellar, Y. Grinkova, V.W. Langenfeld, D. Swedien, J. Stamschror, J. Alvarez, F. Luna, A. Gálvan, J. Wulfkuhle, R. Gallagher, B. Norris, C. Flory, M. G. O'Sullivan

Analysis and interpretation of data: D.A. Potter, Z. Guo, I.F. Sevrioukova, E. Petricoin, Q. Cao, H. Chu, J. Lipscomb, K. Gupta, A. Kelekar, I.A. Blair, C.A. Lange, J. Capdevila, J. R. Falck, S.G. Sligar, T.L. Poulos, E. Ambrose, R.J. Schumacher, G. Georg

Writing, review and/or revision of the manuscript: D.A. Potter, Z. Guo

Administrative, technical or material support (i.e., reporting or organizing data, constructing databases): J. Wulfkuhle, R.I. Gallagher, C. Petricoin, T-L. Chu, X. Zhang, Y.K. Bae, G. O'Sullivan, W.M. Atkins, J.H. Capdevila, J.R. Falck

Study supervision: D.A. Potter

Competing Interests: DT is a consultant for Resonant Therapeutics. There is an HBB use patent application (UMN) and an EET-C22 patent (Medical College of Wisconsin and the University of Texas Southwestern Medical Center).

[10]Vanderbilt University, Nashville, TN

[11]University of Texas Southwestern, Dallas, TX

Summary

The mechanisms by which cancer cell-intrinsic CYP monooxygenases promote tumor progression are largely unknown. CYP3A4 was unexpectedly associated with breast cancer mitochondria and synthesized arachidonic acid (AA)-derived epoxyeicosatrienoic acids (EETs), which promoted the electron transport chain/respiration and inhibited AMPKα. CYP3A4 knockdown activated AMPKα, promoted autophagy, and prevented mammary tumor formation. The diabetes drug metformin inhibited CYP3A4-mediated EET biosynthesis and depleted cancer cell-intrinsic EETs. Metformin bound to the active site heme of CYP3A4 in a co-crystal structure, establishing CYP3A4 as a biguanide target. Structure-based design led to discovery of *N1-hexyl-N5-benzyl-biguanide* (HBB), which bound to the CYP3A4 heme with higher affinity than metformin. HBB potently and specifically inhibited CYP3A4 AA epoxygenase activity. HBB also inhibited growth of established ER+ mammary tumors and suppressed intratumoral mTOR. CYP3A4 AA epoxygenase inhibition by biguanides thus demonstrates convergence between eicosanoid activity in mitochondria and biguanide action in cancer, opening a new avenue for cancer drug discovery.

eTOC

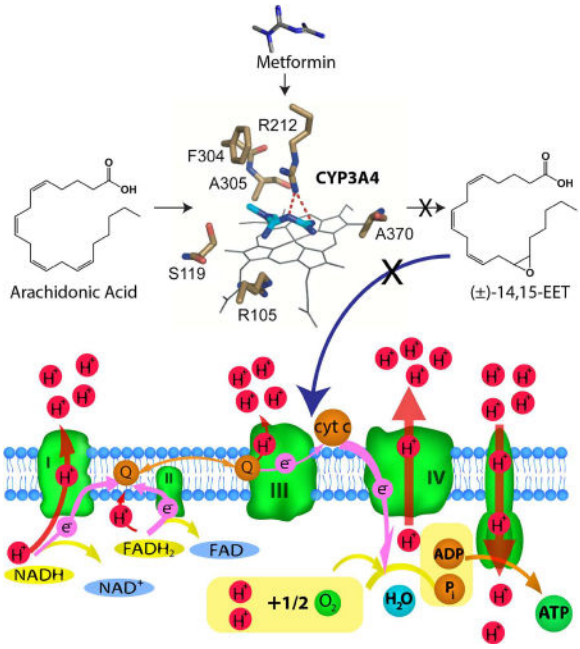

Guo et al. discover inhibition of CYP3A4 AA epoxygenase by biguanides, thereby demonstrating convergence between eicosanoid activity in mitochondria and biguanide action in cancer, opening a new avenue for cancer drug discovery.

Keywords

Cytochrome P450; CYP3A4; epoxyeicosatrienoic acid; mitochondria; autophagy; metformin; biguanide; electron transport chain; hexyl-benzyl-biguanide; breast cancer

Introduction

Cancer cell-intrinsic cytochrome P450 (CYP) epoxidation of arachidonic acid (AA), which generates epoxyeicosatrienoic acids (EETs), is required for ER+HER2− breast cancer cell proliferation *in vitro*, in part, through EET-mediated Stat3 activation (Mitra et al., 2011); however, it is unknown whether cancer cell-intrinsic CYPs promote mammary tumor growth *in vivo*. Certain CYPs, such as CYP2J2, CYP2C8, CYP3A4 and others, are known to synthesize EETs and have been linked to breast cancer progression through promotion of cancer cell proliferation or angiogenesis (Jiang et al., 2005; Jiang et al., 2007; Mitra et al., 2011; Panigrahy et al., 2012; Pozzi et al., 2010). CYP2J2 and CYP2C8 are predominantly expressed in the tumor microenvironment, while breast cancer cell intrinsic CYPs CYP3A4 and CYP2C8 are known to be required for proliferation in ER+ breast cancer (Mitra et al., 2011). Most interest related to EETs in cancer has focused on vascular CYPs. Vascular EETs of endothelial cell origin have been implicated in tumor angiogenesis and escape from dormancy (Panigrahy et al., 2012; Pozzi et al., 2010). Furthermore, inhibition of soluble epoxide hydrolase (sEH), which hydrolyzes EET epoxides and neutralizes their activity, may contribute to tumor progression (Wang and Dubois, 2012). Nonetheless, targeting CYPs expressed in tumor epithelial cells may be of greater interest compared to vascular CYPs, because they may be more tumor-specific. Lack of mechanistic understanding of the roles of cancer cell CYPs and their EET products, including the sites and mechanisms of intracellular action in tumor growth, has prevented development of therapies that target this pathway.

While roles of CYPs in cancer cell respiration are unknown, the discovery of CYP enzymes and sEH in mitochondria (Addya et al., 1997; Labitzke et al., 2007) suggested a new site of CYP activity, but whether and how these observations may be relevant to mitochondrial function was unclear. More recently, EETs have been implicated in the mitochondrial function of cardiac myocytes (Katragadda et al., 2009). The discovery that CYP2J2 transgenic mice attenuate doxorubicin-mediated cardiac damage by protecting mitochondria (Zhang et al., 2009) suggested that EETs may not only promote breast cancer resistance to stress, but also promote the function of cancer cell mitochondria. While CYP2J2 does not appear to be widely expressed in breast cancer, CYP3A4 appears to be associated with breast cancer and widely expressed (Murray et al., 2010). CYP3A4 expression in breast cancer has also been recently associated with risk factors for breast cancer development and progression (Floriano-Sanchez et al., 2014) and is increased in breast tumors, but is also widely expressed in normal mammary tissue (Kapucuoglu et al., 2003). Breast cancer is also an admixture of malignant epithelia, stroma, blood vessels, and, not uncommonly, ductal carcinoma in situ (DICS). Our discovery that CYP3A4 is a highly active AA epoxygenase enzyme and expressed in ER+HER2− and triple negative breast cancer cell lines, where it is required for cell proliferation (Mitra et al., 2011), raised the following questions: i. Is

CYP3A4 widely expressed in breast tumor epithelia and is it associated with mitochondria? ii. Does CYP3A4 regulate the respiration of breast cancer epithelia, thereby revealing a potential breast cancer target? We therefore designed our studies to address these questions, which if answered in the affirmative, could lead to strategies to inhibit breast cancer cell respiration by targeting CYP3A4.

While gene silencing of CYP3A4 revealed that this enzyme promotes Stat3 signaling via EET biosynthesis (Mitra et al., 2011), we lacked chemical probes to determine the impact of immediate CYP3A4 inhibition on signaling and metabolism, thereby allowing us to translate CYP3A4 AA epoxygenase inhibition to the clinic. To develop appropriate chemical probes, which we define as inhibitors of CYP AA epoxygenase activity, we started with metformin, which inhibits CYP3A4-mediated drug metabolism (Choi and Lee, 2012) and is active in breast cancer inhibition (Zakikhani et al., 2006). Similar to CYP3A4 silencing (Mitra et al., 2011), metformin was also found to inhibit Stat3 signaling in breast cancer (Deng et al., 2012), suggesting that metformin might inhibit CYP3A4 mediated EET biosynthesis. Metformin inhibits mammary tumor growth (Iliopoulos et al., 2011; Ma et al., 2014), suppresses mitochondrial respiration (Wheaton et al., 2014) and can be modified easily by click chemistry using the cyano-guanidine condensation reaction (Choi et al., 2016; Kim et al., 2012b; Row et al., 2016). Nonetheless, metformin lacks potency, particularly in ER +HER2− breast cancer (Ma et al., 2014), and potency can't yet be improved by structure activity studies, because a structural target for metformin remains to be identified. We reasoned that we could potentially solve this problem by testing the hypothesis that metformin physically interacts with CYP3A4 and thereby inhibits AA epoxygenase activity. If so, we could then modify metformin to design chemical probes that more potently and specifically inhibit CYP3A4 AA epoxygenase activity and use those probes to test potential roles of CYPs in the regulation of cancer cell respiration.

Results

CYP3A4 and ERα Expression Correlate in Breast Cancer

While CYP3A4 promotes the growth of ER+ breast cancer cells *in vitro* through EET biosynthesis (Mitra et al., 2011) and its expression has been associated with ER+ breast cancer (Murray et al., 2010), it remains unknown whether CYP3A4 is expressed by ER+ breast cancer epithelia. Immunofluorescence analysis of breast tumor cores of unselected consecutive patients (Bae et al., 2012; Kim et al., 2012a) showed cytoplasmic localization of CYP3A4 (Fig.S1a). Moreover, cytoplasmic CYP3A4 was associated with nuclear ERα (Pearson correlation coefficient of r=0.7575; n=48; P-value < 0.0001; Fig.S1b). This result provided a strong rationale to investigate potential roles of CYP3A4 in the progression of ER+ breast cancer.

CYP3A4 Nanodiscs Synthesize EETs, While CYP3A4 Maintains EETs in Breast Cancer Cells and Functions under Low pO2

In addition to genetic methods, chemical probes for CYP3A4 AA epoxygenase function were needed, along with methods to confirm their physical association with CYP3A4. CYP3A4 nanodiscs provide a facile approach to i. confirm that purified recombinant

CYP3A4 indeed synthesizes EETs and ii. provide a spectroscopic assay for the interaction of chemical probes with CYP3A4 (Denisov et al., 2007; Grinkova et al., 2010; Nath et al., 2007). CYP3A4 nanodiscs are self-assembled monodisperse lipid bilayer discs each bearing a single functional CYP3A4 enzyme, allowing spectroscopic assay of heme binding chemical probes. CYP3A4 nanodiscs synthesized EETs in an NADPH and oxidoreductase (CPR) dependent fashion (Fig.1a), confirming that purified full-length CYP3A4 has significant AA epoxygenase activity, similar to CYP2C8 and CYP2J2 (Mitra et al., 2011).

We next measured cellular EET levels in the independently isolated CYP3A4 knockdown MCF-7 lines 4–14 and 3–18, which have 40 and 60% reduction of CYP3A4 (Mitra et al., 2011). Cellular EETs were reduced in both CYP3A4 knockdown lines in terms of total EET levels and individual EET regioisomers (Fig.1b). The cell line exhibiting the most stringent CYP3A4 knockdown, 3–18, exhibited the lowest EETs.

To determine biological relevance, we measured whether CYP3A4 AA epoxygenase activity occurs at O_2 concentrations characteristic of the tumor microenvironment (5–50 μM) (Kallinowski et al., 1989; Ward, 2008). Using an oxygen electrode, we measured the O_2 K_m of CYP3A4 to be 21.6 μM, which is within the range of intratumoral pO_2 (Fig.1c). These results show that CYP3A4 synthesizes EETs, determines EET levels in breast cancer cells and exhibits AA epoxygenase activity under oxygenation conditions consistent with intratumoral pO_2.

CYP3A4 Silencing is Associated with Delayed Escape from Tumor Dormancy

While vascular CYPs and exogenously supplied EETs have been implicated in escape of xenograft tumors from dormancy (Panigrahy et al., 2012), it is not known whether cancer cell-intrinsic CYPs may be required for tumor growth. We therefore tested the effect of CYP3A4 shRNA knockdown on tumor formation in the ER+HER2− MCF-7 orthotopic mammary fat pad tumor model. The MCF-7 cell line is dependent on CYP3A4 and EETs for proliferation *in vitro* (Mitra et al., 2011). We compared growth of tumors derived from the most stringent MCF-7 CYP3A4 knockdown cell line, 3–18, with those derived from a scrambled non-target shRNA cell line NT2 (Mitra et al., 2011). The NT2 tumors with scramble shRNA escaped from dormancy after day 30, whereas the 3–18 tumors were not palpable even by day 45 (Fig.1d), although nodules ≤ 1 mm were detected by microscopy in each fat pad injected with 3–18 cells. CYP3A4 knockdown tumors exhibited central necrosis (5 of 6 evaluable mice), whereas the NT2 tumors did not (0 of 6 evaluable mice; Fig.1e). The MCF-7 breast tumor model therefore requires cancer cell-intrinsic CYP3A4 for escape from dormancy.

CYP3A4 Co-localizes with Breast Cancer Cell Mitochondria

To determine possible roles of CYP3A4 in tumor growth, we focused on regulation of bioenergetics. Notably, certain CYP enzymes can localize to mitochondria (Addya et al., 1997) and EETs have been implicated in stabilization of mitochondrial function in cardiac myocytes (El-Sikhry et al., 2016; Katragadda et al., 2009). To test subcellular localization of CYP3A4, the full-length CYP3A4 protein was stably over-expressed in the MCF-7 cell line C14 and compared with an MCF-7 empty vector control line, P7. Co-staining for CYP3A4

(fluorescein secondary antibody in green) and MitoTracker Red© (red) revealed more intense co-localization (yellow) of CYP3A4 and mitochondria in perinuclear regions in C14 cells (lower panels) compared to P7 cells (upper panels) (Fig.1f right panel; western quantitation of CYP3A4 over-expression left panel). These results show that CYP3A4 localizes to breast cancer mitochondria.

EET Stabilization Promotes Mitochondrial Function

To determine whether endogenous EETs influence mitochondrial function in breast cancer cells we measured their effects on the oxygen consumption rate (OCR), an indicator of mitochondrial respiration, and the extracellular acidification rate (ECAR), an indirect measure of lactate production. To transiently elevate intracellular EET levels in breast cancer cells, we first used t-AUCB, which is an inhibitor of soluble epoxide hydrolase (sEH) (Hwang et al., 2006). sEH is known to hydrolyze EETs to less active dihydroxy-EETs, while inhibitors of this activity (sEHi's) increase EET levels in cells and animals (Merabet et al., 2012). t-AUCB treatment increased OCR in MCF-7 cells within 15 minutes in a dose-dependent fashion and this effect was sustained to the 250 minute endpoint ($P=0.0244$ for 2.5 μM and 0.0033 for 5.0 μM t-AUCB; Fig.1g, left panel). Similar results were observed for the triple negative MDA-MB-231 cell line treated with t-AUCB ($P=0.023$ for 2.5 μM and 0.00080 for 5.0 μM t-AUCB) (Fig.S1c, left panel). Notably, no effect of t-AUCB was observed on the ECAR in either cell line (Fig.1g, right panel; Fig.S1c, right panel). These results support a model in which CYP AA epoxygenase activity primarily regulates OCR and does so in a stimulatory fashion.

However, t-AUCB only stabilizes endogenous EETs. To more directly assess whether EET modulation affects mitochondrial function, we treated MCF-7 cells with a non-hydrolysable, non-ester-forming EET analog, EET C22, resistant to the cellular processing to which exogenous EETs are subject (Fig.S1d). Similar to EET, EET C22 causes aortic ring relaxation, a standard assay for EET activity (Drs. John Imig and John Falck, personal communication) (Falck et al., 2014). EET C22 promoted MCF-7 cell proliferation (Fig.S1e) similar to (±)-14,15-EET (Mitra et al., 2011). EET C22 accelerated the OCR (Fig.1h, left panel; $P=0.019$) and suppressed the ECAR (Fig.1h, right panel; $P=0.034$). EET C22 had a more potent effect than t-AUCB, possibly because of its agonist activity, compared to t-AUCB, which appears to primarily inhibit sEH. Furthermore, the EET antagonist (±)-14,15-EEZE suppressed OCR and ECAR (Fig.1i; left panel OCR, right ECAR). Suppression of OCR by (±)-14,15-EEZE was associated with early activation of AMP-dependent protein kinase α (AMPKα) (Fig.S1f; western left panel, quantitation right), which is expected with acute inhibition of OCR. Together, the effects on OCR of chemical probes t-AUCB, EET C22 and (±)-14,15-EEZE support a model in which CYP AA epoxygenase activity up-regulates respiration, in part, through EET biosynthesis. The mechanism of ECAR reduction by (±)-14,15-EEZE remains to be determined, but could involve acute reduction of ATP needed for priming of glycolysis.

CYP3A4 Silencing Activates AMPK while (±)-14,15-EET Inhibits AMPK

Previous studies have shown that EETs protect the membrane potential ($\Delta\Psi m$) of cardiac myocytes (Katragadda et al., 2009). We therefore hypothesized that EETs protect

mitochondrial respiration assayed by OCR, while suppressing pro-catabolic AMPK function, assayed in part by ECAR. To determine whether CYP3A4 tonically suppresses phosphorylation of AMPKα on Thr172 (pAMPKα), we determined the phosphorylation status of AMPKα in the MCF-7 CYP3A4 knockdown cell lines 3–18 and 4–14 (Mitra et al., 2011). CYP3A4 silencing in MCF-7 cells was associated with steady-state activation of pAMPKα in both knockdown cell lines (Fig.2a; 3–18, P=0.0013; 4–14, P=0.024). Consistent with this finding, (±)-14,15-EET treatment of MCF-7 cells (1 μM) was associated with suppression of pAMPKα phosphorylation at 6 and 24 hours (Fig.2b; western left panel, quantitation right panel; $P<0.05$ for both time points). In contrast, (±)-14,15-EET had no effect on AMPK phosphorylation in the triple negative breast cancer cell line MDA-MB-231 (Fig.2c; 24 hour time point). These findings are consistent with steady-state suppression of catabolism by CYP3A4 in ER+ breast cancer.

CYP3A4 Silencing Promotes Catabolism

Unexpectedly, CYP3A4 knockdown was associated with increased baseline OCR ($P=8.2\times10^{-5}$ and 3.4×10^{-4}; 4–14 and 3–18) and ECAR ($P=6.0\times10^{-4}$ and 0.020; 4–14 and 3–18) for both CYP3A4 knockdown cell lines (Fig.2d,e). CYP3A4 knockdown also increased spare respiratory capacity 3.0-fold and 1.5-fold for the 4–14 and 3–18 cell lines, as shown by an increased difference of OCR vs. baseline following sequential treatment with oligomycin (ATP synthase inhibition) and FCCP (H+ gradient uncoupling) (Fig.2d,e). Steady-state ATP levels normalized to cell number were increased in the CYP3A4 knockdown lines (Fig.2f), but pAMPKα Thr172 phosphorylation was elevated in this steady state (Fig.2a) indicating over-riding catabolic signals despite elevated ATP levels. Supporting a model in which activation of catabolism is downstream of AMPK activation induced by suppression of AA epoxygenase activity in MCF-7 cells (Fig.2a), the AMPK activator AICAR increased OCR and ECAR in this cell line (Fig.2g; left panel OCR, right ECAR), similar to CYP3A4 knockdown (Fig.2d,e).

The CYP3A4 knockdown cell lines exhibited reduction of the ubiquitin binding autophagosome protein p62 (Sequestosome-1), indicating utilization of p62 and suggesting that CYP3A4 knockdown induces a state of constitutive autophagy (Fig.2h; quantitation middle panel; $P<0.05$ for both cell lines). Furthermore, the ratio of LC3B-II/LC3B-1 was increased by CYP3A4 knockdown also suggesting a state of increased autophagy (Fig.2h; quantitation right panel; $P<0.05$ for both cell lines). Thus, while CYP3A4 knockdown is associated with AMPK activation and increased cellular ATP levels, loss of tumorigenicity is associated with increased catabolism, which produces ATP. These findings strongly support a model in which CYP3A4 promotes breast cancer anabolism through EET biosynthesis.

Metformin Inhibits CYP3A4 and Reduces EETs in ER+ Breast Cancer Cells

Metformin is a well-known activator of AMPK in breast cancer cells (Zakikhani et al., 2006) and inhibits breast tumor growth (Iliopoulos et al., 2011; Liu et al., 2009; Ma et al., 2014). In contrast to AICAR, metformin decreases OCR, inhibits Complex I activity of cancer cell mitochondria (El-Mir et al., 2000; Wheaton et al., 2014), and inhibits mitochondrial glycerophosphate dehydrogenase activity as well (Madiraju et al., 2014). The structural target of metformin remains unknown, but metformin is also a competitive inhibitor of

CYP3A4 drug metabolism (Choi and Lee, 2012). We hypothesized that metformin may activate AMPK, in part, by competing with CYP3A4-mediated metabolism of AA to EETs. We therefore tested whether metformin affects CYP3A4-mediated EET biosynthesis and EET levels in breast cancer cells. Consistent with this novel hypothesis, metformin was found to inhibit NADPH-dependent synthesis of (±)-8,9, (±)-11,12, and (±)-14,15-EET by CYP3A4, exhibiting IC_{50} values of 1.5, 2.2, and 4.5 mM, respectively (Fig.2i). In contrast, the AA epoxygenase activity of CYP2J2, implicated in cancer progression (Jiang et al., 2005; Jiang et al., 2007), was not inhibited by 0.75, 1.5 or 3 mM metformin (data not shown). Furthermore, intracellular EET levels in MCF-7 cells were reduced by metformin (5 mM) after 6 hours of treatment (Fig.2j; $P<0.05$ for each regioisomer). Together, these results suggest that activation of AMPK by metformin may be related to CYP3A4 inhibition.

Metformin Causes a Spectral Spin Shift on CYP3A4

To determine whether there is a physical association between metformin and CYP3A4, we used CYP3A4 nanodiscs to measure a spectral shift of the Soret band, thereby providing physical evidence of the interaction of metformin with the heme ring in the active site of CYP3A4 (Denisov et al., 2007; Grinkova et al., 2010; Nath et al., 2007). Interaction of metformin with CYP3A4 nanodiscs resulted in a type I spin shift trough at 415 nm (Fig.2k; left panel), exhibiting a spectral dissociation constant of K_s=400 μM (Fig.2k; right panel). The type I spectral shift was observed at high metformin concentrations, which may mean that more than one metformin molecule can potentially pack in the active site and partially displace water coordinating to the heme iron. When metformin was incubated with a soluble, truncated form of CYP3A4 (Δ3–22) lacking the hydrophobic N-terminal domain, a type II spin shift was observed with a peak at 433 nm and a spectral dissociation constant of K_s=2 μM (Fig.S2a). The type II spin shift observed with CYP3A4 (Δ3–22) may mean that metformin can either coordinate to the heme iron or somehow change the water molecule coordination to the heme iron in the soluble N-terminal truncated CYP3A4 protein. We also confirmed that metformin does not inhibit the transfer of electrons from cytochrome CPR by measuring the rate of reduction of cytochrome c by CPR (Fig.S2b). These results support the hypothesis that metformin activity in MCF-7 cells is directly related to its binding of the CYP3A4 heme.

Metformin Co-crystalizes in the CYP3A4 Active Site and Binds to the Heme

Metformin was successfully co-crystalized with a soluble, truncated form of CYP3A4 (Δ3–22) enabling the X-ray structure to be solved to a resolution of 2.6 Å (Fig.2l, Table S1). Metformin was positioned over the heme and was also close enough to R212 in the F-F' loop for H-bonding interactions. This co-crystal illustrates the flexibility of the CYP3A4 active site tertiary structure, particularly in the F-F' loop, where the distance from the distal nitrogen of R212 to the heme iron is 18.5 Å in the ritonavir co-crystal (3XNU.pdb) and only 6.1 Å in the metformin co-crystal (5G5J.pdb). The adoption of greater sp3 character could possibly lower the pK_a of metformin, especially in the confines of the active site near the heme iron, thereby enabling R212 to H-bond with metformin (Fig.2m) (Fig.2n; stereo view).

N1-Hexyl-N5-Benzyl-Biguanide (HBB) Binds to the CYP3A4 Active Site Heme

We next used the CYP3A4-metformin crystal structure to reverse engineer biguanides expected by structure-based design to be more potent inhibitors of CYP3A4 AA epoxygenase activity. We hypothesized that novel biguanides (neo-biguanides) with higher dock scores than metformin (Fig.3a) could be discovered by *in silico* docking (Jain, 2007) using a feasible chemical space of biguanide compounds (Kim et al., 2012b). The CYP3A4-metformin co-crystal structure was used to dock 18 other biguanides in the active site of CYP3A4 (Table S2). Docking scores were compared using the Surflex Dock program (Jain, 2007), with a higher dock score indicating a more favorable docking interaction. Compound **4** (*N1-hexyl-N5-benzyl-biguanide;* HBB) (Fig.3b) docked with a >2 log higher dock score (score=7.11) than metformin (Fig.S2c vs. d) with close proximity to the heme and at a higher dock score than the other biguanides, except **1** and **2** (Table S2). Of the 5 biguanides with the highest dock scores, syntheses compounds **2** (*N1-hexyl-N5-imidazolyl-biguanide;* HIB), **4** (HBB), and **5** (*N1-hexyl-N5-pyrimidnyl-biguanide;* HPB) were most feasible and therefore performed. HBB was the most potent inhibitor of the MCF-7 cell line (IC_{50}=20 μM) (Table S3) and inhibited ER+ and triple negative breast cancer cell lines with similar IC_{50} values (Table S4). Unlike metformin, a co-crystal of CYP3A4 and HBB could not be obtained despite co-crystallization experiments performed under a range of conditions (Drs. I. Sevrioukova and T. Poulos; unpublished data). Nonetheless, HBB exhibited a strong type I spin shift with CYP3A4 nanodiscs (K_s=110 μM) (Fig.3c,d) and soluble CYP3A4 Δ3–22 (K_s=164 μM) (Fig.S2e,f). The spin shift therefore provided physical evidence of close proximity of HBB and the heme iron of CYP3A4.

HBB Selectively Inhibits CYP3A4 AA Epoxygenase Activity

HBB was tested for inhibition of AA epoxygenase activity of microsomal CYPs: CYP3A4, CYP2C8, and CYP2J2. The IC_{50} values for inhibition of CYP3A4-mediated synthesis of (±)-8,9, (±)-11,12, and (±)-14,15-EET were 9.5, 8.0, and 9.5 μM (Fig.3e). The HBB IC_{50} values for CYP2C8 were significantly higher at 65, 50, and 45 μM (Fig.3f), indicating selectivity of HBB for CYP3A4. HBB did not inhibit the AA epoxygenase activity of CYP2J2 (data not shown). HBB can therefore be used as a selective chemical probe for CYP3A4 epoxygenase activity.

(±)-14,15-EET Partially Rescues Biguanide Inhibition of Cancer Cell Growth

While metformin has been linked with inhibition of Stat3 signaling (Deng et al., 2012) and more hydrophobic biguanides such as phenformin have been linked to mitochondrial inhibition (Shackelford et al., 2013), we lack a mechanistic model accounting for both sites of action. While exogenously added (±)-14,15-EET promotes breast cancer growth through Stat3 (Mitra et al., 2011), it may not effectively reach mitochondria because of hydrolysis and esterification (Zeldin et al., 1995), leaving mitochondrial mechanisms unrevealed without more cell penetrating EET analogs. For the MCF-7 cell line, (±)-14,15-EET abrogated most of the growth inhibition by metformin and part of the inhibition by buformin, phenformin and HBB (Fig.3g). The EET analog C22 also partially abrogated HBB inhibition (Fig.3h). (±)-14,15-EET also abrogated most of the HBB inhibition of the ER+ T47D cell line (Fig.3i). In contrast, EETs failed to counteract HBB inhibition of the

triple negative cell lines MDA-MB-231 (Fig.3j) and MDA-MB-435/LCC6 (not shown). The results suggest that biguanides share a common CYP AA epoxygenase inhibitory mechanism. The results also suggest that either ER+ breast cancer cell lines are more dependent on EETs or they are more sensitivity to exogenous EETs.

HBB Strongly Inhibits OCR and Suppresses ATP Stores, while Metformin Does Not

Biguanide inhibition of cancer has been proposed to inhibit mitochondrial O_2 consumption through inhibition of complex I (El-Mir et al., 2000; Wheaton et al., 2014). Metformin treatment of the MCF-7 cell line (2.5 or 5 mM) resulted in marginal suppression of OCR over 5 hours following treatment and a transient ECAR spike, followed by suppression of ECAR (Fig.4a; OCR left panel, ECAR middle). There was no effect of metformin on cellular ATP at 6 hours (Fig.4a; right panel, 10% serum, normalized to cell number). In contrast, HBB treatment resulted in rapid, dose-dependent reduction of OCR within 15 minutes. HBB resulted in > 250-fold more potent inhibition of OCR compared to metformin (Fig.4b; OCR left panel, ECAR middle). HBB also induced a transient spike of ECAR, followed by inhibition without recovery (Fig.4b; middle panel). HBB reduced ATP by 30% at 6 hours (Fig.4b; right panel; $P<0.05$, 10% serum), indicating that in contrast to CYP3A4 knockdown, acute inhibition of CYP3A4 depletes ATP stores. HBB did not reduce breast cancer cell viability at 2 and 4 hours in complete medium (Fig.S3a) nor at 4 hours under conditions used in the efflux analyzer (Fig.S3b), indicating that HBB mediated ATP reduction was due to alteration of metabolism rather than cell death. The potent, neurotoxic complex I inhibitor rotenone (1.0 μM) served as a positive control to demonstrate that the pattern of OCR and ECAR inhibition by HBB is consistent with rapid inhibition of the electron transport chain (ETC) (Fig.S3c; $P<0.0001$ for rotenone effect on OCR and ECAR).

To determine whether HBB induces similar OCR/ECAR profiles in other breast cancer cell lines, T47D, MDA-MB-231, and MDA-MB-435/LCC6 cells were treated with HBB. Similar significant dose-dependent inhibition of OCR and ECAR were observed (Fig.S3d,e,f; HBB vs. DMSO control; endpoint P values all <0.015). These results show that the effects of HBB on OCR and ECAR are less likely cell line specific.

EET Stabilization Promotes Resistance to HBB-Mediated OCR Inhibition

To determine whether HBB suppression of OCR can be opposed by EET stabilization, t-AUCB (5 μM) was added 120 minutes before addition of HBB (5 μM). Pre-treatment with t-AUCB resulted in a 1.5-fold reduction in the rate of OCR decline, but had no effect on ECAR (Fig.4c; OCR left panel, ECAR right). This result indicates that stabilization of EETs protects breast cancer cells from HBB inhibition of OCR.

ΔΨm Depends, in part, on CYP AA Epoxygenase Activity and is Inhibited by HBB

We then asked whether EETs protect the ETC from HBB. Using the indicator dye JC-1 to measure ΔΨm, we tested whether HBB inhibits ΔΨm, in part, through depletion of EETs, which have been reported to stabilize ΔΨm in cardiac myocytes (Batchu et al., 2012; Katragadda et al., 2009). HBB treatment of the MCF-7 and MDA-MB-231 cell lines (20 μM for 4 hours) caused a rapid reduction of ΔΨm ($P<0.05$) (Figs.4d,e MCF-7 cells; Fig.S4a,b MDA-MB-231 cells). The ΔΨm was partly rescued by pre-treatment with exogenous

(±)-14,15-EET (P<0.05 for each) (Fig.4d,e; MCF-7 cells) (Fig.S4a,b; MDA-MB-231 cells). The effect of HBB on ΔΨm was also measured using the mitochondrial dye tetramethylrhodamine ethyl ester (TMRE) under non-quenching conditions and HBB was confirmed to inhibit ΔΨm in a dose dependent fashion (Fig.4f). The linearity of the assay was confirmed (Fig.S4c) and the conditions were confirmed as non-quenching (Fig.S4d). These results indicate that ΔΨm depends, in part, on CYP-mediated EET biosynthesis.

HBB Rapidly Activates pAMPK and Inhibits Stat3, mTOR, and ERK

We then studied the effects of HBB on signal transduction in the MCF-7 cell line, which is EET responsive (Mitra et al., 2011). Depletion of ATP stores by HBB suggested a mechanism impacting the AMPK/mTOR axis. Metformin at high concentrations (10–30 mM) and extended treatment times (24–48 hours) results in AMPK phosphorylation and reduces Stat3 and mTOR phosphorylation (Deng et al., 2012; Zakikhani et al., 2006). In contrast, much lower dosing of HBB (20 μM) activated pAMPKα within 30 minutes, but at 24 hours the effect was greatest, particularly in presence of serum (Fig.5a-c). HBB more rapidly inhibited Stat3 phosphorylation in the presence of serum (Fig.5a–c). HBB treatment also resulted in rapid and transient activation of p70 S6 kinase at 30 minutes (Fig.5a–c), which was independent of serum starvation; this finding shows a novel, stress-related S6 kinase activation, independent of mTOR S2448 phosphorylation. Significant inhibition of mTOR, S6 kinase and ERK by HBB occurred by 24 hours in the presence or absence of serum (Fig.5a–c). Activation of AMPK under conditions of 10% serum and serum withdrawal correlated with mTOR inhibition, consistent with the known inhibitory activity of AMPK on mTOR (Dowling et al., 2007).

HBB Inhibits MCF-7 Xenograft Tumor Growth

HBB was tested for tumor inhibition in orthotopic nude mouse mammary fat pad models of MCF-7 and MDA-MB-231 tumors. A dose of HBB at 4 mg/kg given ip daily beginning the day after tumor cell implantation, was found to be a minimal effective dose (MED) in the MCF-7 model (Fig.6a). At the same HBB dose and schedule, the MDA-MB-231 xenograft tumors exhibited no inhibition (Fig.6b). Weight loss was less than 8% in both models (Fig. 6c,d).

In vitro, MDA-MB-231 cells exhibited greater HBB-mediated induction of reactive oxygen species (ROS) compared to MCF-7 (data not shown). While EETs failed to rescue MDA-MB-231 cells from HBB inhibition (Fig.3j), they were rescued by the antioxidant N-acetyl-cysteine (NAC) (Fig.S5a). In contrast, MCF-7 cells were rescued from HBB by EETs (Fig. 3g), but not NAC (Fig.S5b). These results suggest a correlation between EET rescue of tumor cells *in vitro* and HBB sensitivity *in vivo*, but confirmation is required.

Dose escalation of HBB was performed in the MCF-7 model. At 6 mg/kg dosing, given ip 4 days per week with no more than 2 consecutive days of dosing, (24 mg/kg/week ip), HBB reduced tumor size (Fig.6e; P=0.039). Weight loss was <6% by the end of the study (Fig.6f). On this dose and schedule, tumor weights were half in HBB-treated mice at the end point (Fig.6g; P=0.034). Notably, tumor size measured the day before treatment initiation was well balanced between the two groups (Fig.6h). There were no HBB-related hepatic or

cardiac toxicities found by post-mortem histopathology in either HBB-vs. vehicle-treated mice (not shown) and there were no difference in non-fasting blood glucose levels (data not shown). Cremophor was included in both arms to allow future studies of HBB/chemotherapy combinations.

Correlative Biomarkers of HBB Efficacy in the MCF-7 Xenograft

Reverse phase protein microarray (RPPA) analysis of 155 signaling proteins, after correction for multiple comparisons, revealed two highly suppressed proteins in MCF-7, but not MDA-MB-231, tumors of mice treated with HBB: reduction of mTOR ($P=4.06\times10^{-6}$) and reduction of PKC-ζ/λ phospho-threonine 410/403 (P=0.000119) (Fig.6a, Table S4, MCF-7; Fig.6b, Table S5, MDA-MB-231). Notably, these mTOR and PKC-ζ/λ findings were specific to the tumors and not seen *in vitro*.

Discussion

Our ability to effectively target CYP AA epoxygenase enzymes in cancer has been limited by lack of effective and selective inhibitors. Furthermore, the goal of developing more potent biguanides for breast cancer therapeutics has been impeded by lack of a structural target for metformin. In the present study, we demonstrate converging solutions of these two unsolved problems via a novel strategy for inhibition of ER+HER2− breast cancer. These efforts led to the findings that CYP3A4 is required for tumor growth and localizes to breast cancer cell mitochondria where it promotes respiration, while suppressing autophagy, in part, through EET biosynthesis. The recognition that metformin is a chemical probe for CYP3A4 AA epoxygenase function in breast cancer immediately suggested that the CYP3A4 co-crystal structure could permit the design of more potent chemical probes for AA epoxygenase activity in breast cancer. Three candidates — HIB, HPB, and HBB — were synthesized, of which HBB was the most potent. HBB served as a specific inhibitor of CYP3A4 AA epoxygenase activity and recapitulated the expected effects of metformin *in vitro* and *in vivo*.

CYP3A4 knockdown and the HBB chemical probe allowed us to develop a model in which CYP3A4 exhibits two distinct roles, at the plasma membrane and in mitochondria (Fig.7). It was previously known was that CYPs maintain receptor tyrosine kinase signaling at the plasma membrane through EET biosynthesis (Chen et al., 2001) and that EETs promote proliferation in ER+HER2− breast cancer through Stat3 activation (Mitra et al., 2011) (Fig. 7a, *membrane*). To this model we add that EETs activate the breast cancer mTOR pathway (MCF-7 RPPA analysis of EET promotion of phospho-TOR S2448 and eIF4G phospho-S1108; data not shown) (Fig.7a; *membrane*). Genetic studies as well as EET and AMPK agonist/antagonist studies led us to a model in which mitochondrial CYP3A4 promotes respiration, in part, through EET biosynthesis (Fig.7a; *mitochondria*). Our results support dual roles of CYP3A4 in Stat3 signaling and mitochondrial respiration. In our model, membrane EETs activate Stat3 while mitochondrial EETs activate OCR and attenuate ECAR, which in part reflects glycolytic activity. How these sites of EET action are coordinated remains to be determined, but this model suggests there may be two EET pools, membrane and mitochondrial. The most important implication of this model is that CYP3A4

AA epoxygenase activity may be a regulator of anabolism through mTOR activation (Fig. 7a).

As a chemical probe, HBB provides new information about immediate early and late events related to disruption of mitochondrial respiration and about OCR/ECAR balance and signal transduction. Regardless of ER status, HBB treatment results in immediate early suppression of OCR and a transient spike of ECAR, similar to rotenone, suggesting that this is a pattern characteristic of potent disruption of the ETC (Fig.7b). In this model, early HBB-mediated loss of EET biosynthesis also results in reduction of Stat3 and mTOR signaling at the membrane and activation of AMPK, resulting in suppression of mTOR phosphorylation (Fig.7b). The reasons for the early ECAR spike and sustained loss of ECAR following the spike remain to be determined.

These studies support a model in which CYP3A4 AA epoxygenase activity regulates the balance between anabolism and catabolism in breast cancer. Silencing of CYP3A4 in breast cancer cells induced a catabolic state and increased ATP, but removed the capacity to form tumors. This finding was remarkable because the increased ATP in CYP3A4 knockdown cells had no inhibitory effect on AMPK; rather, the opposite was observed. With CYP3A4 knockdown, autophagy/catabolism was activated even in the presence of adequate nutrients, in contrast to models where control of autophagy/catabolism is coupled to glucose availability (Kim et al., 2011). In this model, inhibition of AMPKα by EETs may be due to increased respiration or another, as yet unknown, mechanism. CYP-mediated AMPKα inhibition could provide a novel mechanism through which CYPs activate mTOR and function as a “brake” on cellular catabolism. In breast cancer, EETs appear to be acting in the opposite direction compared to cardiac myocytes, where they activate AMPKα2 (Wang et al., 2016). In cardiac myocytes, EETs improve viability and colony formation through activation of autophagy and respiration (Samokhvalov et al., 2013). Notably, the AMPK phospho-T172 antibody used in our studies does not distinguish between AMPK isoforms.

Unexpectedly, AMPK activation by HBB *in vitro* did not predict tumor response to HBB *in vivo*. *In vitro*, HBB activated AMPKα in MCF-7 and MDA-MB-231 (data not shown) cells. *In vivo*, HBB failed to activate AMPKα in MCF-7 tumors where tumor response was seen but did activate AMPKα in MDA-MB-231 tumors where no tumor response was observed. In contrast, HBB did reduce total mTOR levels in MCF-7 tumors and in MDA-MB-231 tumors, there was marked trend to reduction. It has recently been discovered that suppression of mTOR levels by miRNA 100 sensitizes MCF-7 tumors to paclitaxel (Zhang et al., 2016). By lowering mTOR levels, HBB may sensitize thereby breast tumors to paclitaxel.

These studies provide a blueprint for the use of genetics and chemical biology to target intratumoral CYP AA epoxygenase enzymes in breast cancer. The power of biguanide click chemistry should allow the development of a new class of chemical probes for the functions of CYP3A4 AA epoxygenase in membranes and mitochondria.

Significance

Until now there has been no structural target for metformin in cancer which would inform us on how to rationally develop more potent biguanide chemical probes and analogs for cancer treatment. Furthermore, CYPs were not known to regulate the ETC. Our discoveries of a CYP inhibitory mechanism for metformin in ER+HER2− breast cancer and a metformin/CYP3A4 co-crystal structure together provide an avenue for breast cancer drug development. HBB, derived by reverse engineering of metformin, is a prototype for novel neo-biguanide inhibitors of CYP3A4 AA epoxygenase activity. These inhibitors can be used as chemical probes of CYP regulation of mitochondrial respiration. HBB serves as proof of concept that potent neo-biguanides can be rationally developed to target breast cancer using structural biology methods. HBB or similar compounds of acceptable toxicity can potentially be moved forward to breast cancer clinical trials.

STAR ⋆ METHODS

Contact for Reagent and Resource Sharing

Further information and requests for reagents may be directed to, and will be fulfilled by the corresponding author David A. Potter (dapotter@umn.edu)

Experimental Model and Subject Details

Mice—Animal studies were performed according to an Institutional Animal Care and Use Committees (IACUC)-approved protocol 1505-32594A and monitoring by veterinary staff. For the xenograft studies, female athymic nude mice (Foxn1nu/Foxn1nu) at 4–6 weeks of age were used.

Cell Lines—MCF-7, MDA-MB-231 cell lines were a gift of Dr. Harikrishna Nakshatri (Indiana University) and short tandem repeat profiling (STR) verified by his laboratory. For xenograft experiments testing HBB activity, we used tumorigenic, estradiol responsive MCF-7 cells that were a gift from Dr. Deepali Sachdev (University of Minnesota) and short tandem repeat (STR) profiling verified by her laboratory. Their profile was similar to MCF-7 cells in ATCC, DSMZ, or JCRB databases. T47D cells were purchased from the American Type Culture Collection (ATCC; Manassas, VA). MDA-MB-435 (LCC6) cells were obtained from Dr. Deepali Sachdev (University of Minnesota) and were a gift of Dr. Robert Clarke (Georgetown U.) and confirmed by STR. The MCF-7 cells used in xenograft studies were tested and found to be free of mycoplasma (Lonza). The MDA-MB-231 cells used for in vitro and xenograft studies were tested for pathogens by the RADIL Reference Laboratory (University of Missouri) (now IDEXX BioResearch) and were found to be free of viral pathogens and mycoplasma.

METHOD DETAILS

Chemicals and Reagents

DMEM (low glucose; 1 g/L) was purchased from GIBCO/Invitrogen (Carlsbad, CA). Charcoal-and dextran-stripped serum was purchased from Hyclone (Logan, UT). FBS was

assayed by our laboratory and found to exhibit EET levels of <100 nM. EETs were provided and purified by Drs. Jorge Capdevila (Vanderbilt University), John Falck (University of Texas Southwestern) or purchased from Biomol International (Plymouth Meeting, PA) or Cayman Chemical Co. (Ann Arbor, MI). EET C22 analog was provided by Dr. John Imig (Medical College of Wisconsin) and Dr. John Falck (UT Southwestern). Phenomenex Luna C18 (250 × 0.5 mm, 5-μm particle size) column was purchased from Phenomenex (Torrance, CA). Insect cell microsomes expressing recombinant human P450 CYP3A4 and CYP2C8 (Supersomes™) were purchased from Corning (Corning, NY). JC-1 mitochondrial membrane potential probe was purchased from Thermo Fisher Scientific (Waltham, MA). XF Assay Kit and Mito Stress Kit, both 24 well, were purchased from Seahorse Bioscience (North Billerica, MA). Eicosanoid mass spectrometry standards (±)-8,9-(5Z,11Z,14Z)-EET, (±)-11,12-(5Z,8Z,14Z)-EET, and (±)-14,15-(5Z,8Z,11Z)-EET were purchased from Biomol International (Plymouth Meeting, PA). Arachidonic acid and *d*8-EETs were purchased from Cayman Chemical Co. (Ann Arbor, MI). Methylene chloride, NADPH, EDTA, HPLC-grade acetonitrile, and diethyl ether were purchased from Sigma. HPLC-grade hexane, isopropyl alcohol, and ethanol were obtained from Fisher. ACS-grade ethanol was obtained from Pharmco (Brookfield, CT). TMRE-Mitochondrial Membrane Potential Assay Kit was purchased from Abcam (Cambridge, MA). ATPlite Luminescence Assay System was purchased from PerkinElmer (Waltham, MA). Subcutaneous 17-β-estradiol pellets (0.72 mg/60 day) were purchased from Innovative Research of America (Sarasota, FL).

Antibodies

The following antibodies were from Cell Signaling Technology, Inc. (Danvers, MA): phospho-mTOR (Ser2448) (D9C2) XP® rabbit mAb #5536; mTOR antibody rabbit polyclonal antibody #2972; phospho-p70 S6 kinase (Thr389) antibody #9205 rabbit polyclonal antibody; p70 S6 kinase antibody #9202 rabbit polyclonal antibody; #4188 phospho-AMPKα (Thr172) (D79.5E) rabbit mAb (recognizes α1 and α2 subunits); AMPKα antibody #2532 rabbit polyclonal antibody; phospho-Stat3 (Tyr705) (D3A7) XP® rabbit mAb #9145; Stat3 (124H6) mouse mAb #9139; phospho-p44/42 MAPK (Erk1/2) (Thr202/Tyr204) (D13.14.4E) XP® rabbit mAb #4370; p44/42 MAPK (Erk1/2) antibody #9102 rabbit polyclonal antibody; and β-Actin (13E5) rabbit mAb #4970. The following antibody was from Xenotech, LLC (Kansas City, KS): anti-CYP3A4, rabbit polyclonal antibody, #PWB3A4.

MCF-7 CYP3A4 Over-Expressing Cell Lines

CYP3A4 over-expressing lines were isolated by transfecting MCF-7 cells (parental cells were a gift of Dr. H. Nakshatri; Indiana U.) with a pcDNA3.1 vector encoding a myc-His6 tag and the CYP3A4 open reading frame. Transfections were performed using the FuGENE™ transfection reagent according to manufacturer's instruction (Promega, Madison, WI). MCF-7 cells were seeded in poly-D-lysine coated 6-well plates. Transfection reactions were plated on 100-mm tissue culture plates at 500 cells/plate in complete media with G418 at 600 μg/ml for selection. After two weeks, visible and well isolated surviving colonies were picked with the cloning ring/trypsin method and grown in a 48-well plate and then a 100-mm tissue culture plate once 60% confluency was reached. CYP3A4 expression levels of clones were compared by Western blot.

Immunofluorescence Microscopy

MCF-7 cells stably over-expressing CYP3A4 were seeded on fibronectin-coated cover slips and incubated with 100 μM MitoTracker (red, Invitrogen, San Diego, CA) in dark for 30 minutes the next day. Cells were fixed with 4% paraformaldehyde in PBS and permeabilized with 0.1% Triton-100. After blocking with donkey serum, fixed cells were probed with polyclonal rabbit anti-human CYP3A4 primary antibody (XenoTech LLC, Kansas City, KS) followed by wash, blocking and incubation with FITC-conjugated anti-rabbit IgG secondary antibody (green). Cover slips were then washed, dried and mounted on slides. Fluorescence images were acquired using an Olympus 1×70 microscope fitted with an Olympus DP70 digital camera (Olympus, Tokyo, Japan). Green and red fluorescent images from the same view field were merged with the manufacturer's accompanying software, DP Manager. Yellow color indicates overlapping of red and green fluorescent light. A pcDNA3 vector control line was analyzed as control. The secondary antibody resulted in no significant background fluorescence in the absence of the primary CYP3A4 antibody.

Measurement of OCR and ECAR

Cells were maintained in growth medium consisting of 10% FBS at 37°C with 5% CO_2 and seeded at 100,000 cells per well in XF24-well cell culture microplates (Seahorse Bioscience, North Billerica, MA). Assays were performed in the XF Extracellular Flux Analyzer (Seahorse Bioscience), which measures uptake and excretion of metabolic end products in real time. Oxygen consumption rate (OCR) and extracellular acidification rate (ECAR) were measured using an XF Assay Kit. OCR is reported in pmoles/minute and ECAR in mpH/minute. Before analysis, the cells were switched from culture medium to 0.5 ml XF assay medium (a non-buffered medium including 2 mM L-glutamine but no sodium bicarbonate (buffering agent), glucose, or sodium pyruvate). After baseline measurements, 75 μl assay medium containing control vehicle or drugs were injected into corresponding wells. OCR and ECAR were measured at 18-minute intervals.

We initially used an end point Student t test to measure the significance of difference between curves in OCR and ECAR experiments. To confirm more general differences for the curves over time, we used SAS procedure NLMIXED, a non-linear mixed model, to fit the data. For example, assuming ECAR follows an exponential rate of change, we considered a lognormal model. log(ECAR) a0+(b0+b1*(group=2))*min where a0 is the estimate of ECAR at baseline, b0 is the estimate change every minute and b1 is the estimate change between two groups at same time point. The end point t test was in agreement with pairwise curve comparisons in terms of significance evaluation.

Cellular ATP by Luminescent Assay

Cells were seeded in a 96-well tissue culture plate in 100 μL medium per well. After treatment with either vehicle or testing compound for an appropriate length of time, 50 μL mammalian cell lysis solution was added to each well and the plate was shaken for 5 minutes on an orbital shaker. To each well, 50 μL luminescent substrate and luciferase solution were then added. After incubation in the dark for 10 minutes, luminescence was measured. Cellular ATP levels were then calculated against a standard curve generated with ATP standards of known concentration.

Binding of Biguanides to CYP3A4 Nanodiscs

Substrate titration experiments were performed at 1 μM concentration of CYP3A4 in nanodiscs using a Cary 300 spectrophotometer (Varian, Lake Forest, CA) at 21 °C. Incorporation of CYP3A4 in POPC nanodiscs was done following standard protocols described earlier (Luthra et al., 2013).

CYP3A4 Co-crystal X-Ray Crystallography

The Δ(3–22)CYP3A4 protein was co-crystallized with metformin at room temperature by a microbatch method under oil. CYP3A4 (115 mg/ml) in 50 mM phosphate, pH 7.4, 20% glycerol, and 100 mM NaCl was incubated for 20 min with a 40-fold excess of metformin. Prior to mixing with CYP3A4, pH of the aqueous metformin solution was adjusted to 7.0 with concentrated HCl. After removal of the precipitate by centrifugation, 0.4 microliters of the protein solution was mixed with 0.4 microliters of 12% PEG 3350 and 0.1 M sodium acetate pH 7.0, and the drop was covered with paraffin oil. Crystals were harvested 3 days later and cryoprotected with Paratone-N before freezing in liquid nitrogen. X-ray diffraction data were collected at −170 °C at the Stanford Synchrotron Radiation Lightsource (SSRL) beamline 7-1. The atomic coordinates were deposited in the Protein Data Bank with the ID code 5G5J.

MCF-7 CYP3A4 shRNA Cell Line Xenograft Model

The CYP3A4 shRNA cell line 3–18 and scramble control line NT2 were isolated and grown as previously described, derived from MCF-7 cells (parental cells were a gift of Dr. H. Nakshatri, Indiana U.) (Mitra et al., 2011). The growth of these cell lines in a nude mouse model was performed under IACUC protocol 1302-30326A. Female athymic nude mice (*Foxn1*^{nu}/*Foxn1*^{nu}) at 4–6 weeks of age were used. The cell lines were tested for tumor formation in the right mammary fat pad of nude mice, with estradiol supplementation by timed-release pellet. For the MCF-7 xenograft, 3×10^6 cells in log phase growth were placed in the right 2nd mammary fat pad using a 25-gauge needle on day 0. β-estradiol (E2) was given by a subcutaneous 0.72 mg, 60-day release 17β-estradiol pellet implanted the day before tumor implantation. Tumor modeling was performed using Gompertzian curve fitting with a non-zero baseline to allow use of this model. The mammary fat pad was harvested en bloc after animal sacrifice by isoflurane anesthesia followed by cervical dislocation, and the resection specimen was inked and oriented and placed in tissue block holders with sponges. After formalin fixation and paraffin embedment, the blocks were serially sectioned and examined for tumor by H+E staining.

MCF-7 and MDA-MB-231 Xenograft Models

Animal studies were performed according to an IACUC-approved protocol 1505-32594A and monitoring by veterinary staff. For the xenograft studies, female athymic nude mice (*Foxn1*^{nu}/*Foxn1*^{nu}) at 4–6 weeks of age were used. The mice were weighed twice weekly from receipt to the end of the study and nutrition and behavior were monitored by veterinary staff and technicians. Tumorigenic MCF-7 (gift of Dr. Deepali Sachdev; U. Minnesota) and MDA-MB-231 (gift of Dr. Harikrishna Nakshatri; Indiana U.) cell lines responsive to EETs were previously published (Mitra et al., 2011). The MCF-7 cells were tested and confirmed

to be estradiol responsive *in vitro* (data not shown). For the treatment with daily dosing (Fig. 6a,b) dose escalation of HBB from 2 mg/kg to 12 mg/kg daily by ip injection was performed to find an MTD for daily dosing of 4 mg/kg. This MTD for daily dosing was also a minimal effective dose (MED). For the MCF-7 xenograft dosed at 6 mg/kg HBB, 5.1×10^6 cells in log phase growth were placed in the right 2nd mammary fat pad using a 25-gauge needle on day 0. For the MCF-7 xenograft dosed at 4 mg/kg HBB, 3.8×10^6 cells in log phase were injected in the right 2nd mammary fat pad. 17-β-estradiol (E2) was given at 1 μM in drinking water at beginning the day of tumor implantation. Randomization was performed prior to treatment using the web program http://www.randomizer.org. Tumor measurements were taken with a digital caliper twice weekly and thereafter at the same time that weights were recorded. Tumor volumes were determined by the formula: volume=length × $[\text{width}]^2/2$. Tumors were collected from each mouse after sacrifice and end-point tumor weights were measured. For the MDA-MB-231 xenograft model, the procedures were similar, but mice were injected with 1×10^6 cells in the right 2nd mammary fat pad and no estradiol was used in the drinking water. In both experiments, the mice were randomized the day after tumor cell injection. Euthanasia was performed by isoflurane anesthesia followed by cervical dislocation for all mice at the study endpoint unless an individual mouse met euthanasia criteria prior to this time. Tumors were harvested after sacrifice and bisected, with half placed in formalin for histology and half in (Optimal Cutting Temperature) OCT compound for reverse phase array analysis.

The MTD for daily dosing was found by two-fold dose escalation. An HBB dose of 8 mg/kg/day ip in cohorts of 5 tumor-bearing mice resulted in animal deaths within 3 days and was reduced to 4 mg/kg/day ip. The initial studies were performed with ip treatment with HBB at the MTD or with PBS beginning on day 1. Twenty mice per arm was used for each study; error bars represent SEM. Significant weight loss was observed for the MCF-7 and MDA-MB-231 models after initiation of daily HBB dosing at 4 mg/kg/day ip, but weight loss was no more than 8% for the MCF-7 model noted on day 4 (P=0.00057) and recovered by the end of the study (P=0.59). For the MDA-MB-231 model, end point weight loss was 2.5% (P=0.31). The plasma concentration of HBB was measured 1 hour after the daily dosing (4 mg/kg/day ip) and was 0.53 μM. Detailed pharmacokinetics will be performed in a follow-up study, but may require tissue measurements because tissue levels of metformin are much higher than plasma levels (Chandel et al., 2016; Choi and Lee, 2012).

TMRE ΔΨm measurement

MCF-7 cells were plated in black wall clear bottom 96-well tissue culture plates at 20,000 cells/well and grown overnight. In addition to treatment and no treatment control groups, a non-mitochondrial TMRE staining group was included as background fluorescence control, to which 10 μM of FCCP was added and incubated for 30 minutes at 37 °C. TMRE was then added to all wells at 500 nM. After 30 min incubation at 37 °C, media was removed and cells were washed twice with PBS (0.2% BSA) and 100 μl of PBS (0.2% BSA) was added. Fluorescence was read at Ex 530 nm/Em 590 nm. TMRE fluorescence due to mitochondrial potential was calculated by subtracting the background fluorescence (FCCP group) from total fluorescence.

Optimization of TMRE Staining Conditions

MCF-7 cells were seeded in black wall clear-bottom 96-well tissue culture plate at varied density and grown overnight. To each well, either FCCP 10 μM or DMSO (control) was added and incubated for 30 min at 37 °C followed by the addition of TMRE from 30–1000 nM. After 30 min incubation at 37 °C, media was rem oved and cells were washed twice with PBS (0.2% BSA) and 100 μl of PBS (0.2% BSA) was added. Fluorescence was read at Ex 530 nm/Em 590 nm. TMRE fluorescence due to mitochondrial potential was calculated by subtracting the background fluorescence (FCCP group) from total fluorescence (control group) and plotted against concentration of TMRE.

Cell Viability Assay

MCF-7 cells were plated in 24-well XF assay plates at 100,000 cells/well in complete media and grown overnight. Growth media was replaced with XF assay media (DMEM, pH=7.4) and treated with either DMSO or HBB. After 4 hours, cells were harvested and counted with trypan blue staining manually under a microscope.

CYP3A4 Nanodisc-mediated EET Biosynthesis

In 1 ml of 100 mM HEPES, pH 7.4, 10 mM $MgCl_2$, 0.1 mM dithiothreitol (DTT) buffer, CYP3A4-nanodisc (ND) and cytochrome P450 reductase (CPR) were added to final concentrations 0.27 μM and 1.15 μM, respectively (1:4 molar ratio). The mixture of CYP3A4-ND and CPR was equilibrated for 10 minutes at 37°C before adding arachidonic acid (55 μM) followed by addition of NADPH (160 μM). The reaction was terminated after 2 minutes by addition of 2 ml of dichloromethane. Samples were centrifuged at 3,000 rpm for 10 min and 0.5 ml of the organic phases were evaporated under a gentle stream of nitrogen. Residues were reconstituted in 20 μl of MeOH containing [^{13}C-20]-EET internal standards and analyzed by LC-ESI-MS/MS (Mitra et al., 2011).

Determination of Oxygen Km for CYP3A4

Human recombinant CYP3A4 Supersomes™ (Corning, NY)-catalyzed epoxygenation of arachidonic acid (AA, 100 μM) reaction was performed at 37°C in the presence o f a NADPH regenerating system. Oxygen concentration of the reaction solution was varied and rates of oxygen consumption were recorded with a YSI 5300 biological oxygen monitor (Yellow Springs Instruments, Yellow Springs, OH). Lineweaver Burke analysis was performed to calculate the oxygen Michaelis-Menten constant (Km).

Rate of Reduction of Cytochrome c

In a quartz cuvette, reduction of cytochrome c reaction was initiated by addition of CPR (final concentration 0.2 mg/mL) to 1 mL potassium phosphate buffer (0.3 M, pH=8.3) containing cytochrome c (62 μM) and NADPH (50 μM). Absorbance at 550 nM was monitored real time by a Cary 50 UV-Vis Spectrophotometer (Agilent, Santa Clara, CA).

Cell Proliferation Assay

To cells grown in 96-well-tissue culture plate, 20 μl/well of 3-(4,5-Dimethylthiazol-2-yl)-2,5-diphenyltetrazolium bromide (MTT) solution (5 mg/ml in PBS) was added. After 1–

2 hours incubation at 37° C, the plate was centrifuge d. Supernatant was discarded and 100 μl DMSO was added to dissolve water insoluble formazan, and the absorbance was read at 540 nm with a plate reader.

LC-ESI/MRM/MS EET Measurement

EETs were measured by an LC-ESI/MRM/MS analytical method on a Thermo Electron Quantum Discovery Max triple quadrupole mass spectrometer (Thermo Finnigan, San Jose, CA) coupled with an Agilent 1100 HPLC (Santa Clara, CA), using argon as the collision gas. Negative ion monitoring was performed at the following diagnostic product ions: 319 m/z → 155 m/z for 8,9-EET; 319 m/z → 179 m/z for 11,12-EET; 319 m/z → 219 m/z for 14,15-EET; 339 m/z → 163 m/z for 8,9-[^{13}C-20]EET; 339 m/z → 233 m/z for 11,12-[^{13}C-20]EET; and 339 m/z → 259 m/z for 14,15-[^{13}C-20]EET. Base-line resolution of EET regioisomers was achieved on a Phenomenex Luna C18 (2) reverse phase capillary column (250 × 0.5 mm, 5-μm particles) using the following mobile phase combinations: isocratic 5% B for 5 min, gradient 5–70% B for 5 min, hold at 70% for 30 min and then 95% for 10 min; A: 0.01% acetic acid in water, B: 0.01% acetic acid in acetonitrile; 10 μl/min flow rate. A standard curve was obtained by linear regression of the peak area ratio of authentic EET regioisomers against internal standards. The amount of EETs in samples was calculated according to the standard curve. The (±)-5,6-EET regioisomer was not measured because it undergoes rapid internal degradation.

EET Extraction from Cells

Cells grown to 50–75% confluence on 150 × 20-mm tissue culture plates were washed twice with cold PBS and collected in 3 ml cold PBS containing 2 μM soluble epoxide hydrolase inhibitor t-AUCB (a gift from Dr. Bruce Hammock, University of California, Davis). After centrifugation at 1,000×rpm for 5 minutes, supernatant was discarded and cells were resuspended in 1 ml cold PBS with 2 μM t-AUCB, to which [^{13}C-20]EET internal standard was added. Total lipids were then extracted with a 2:1 mixture of chloroform and methanol. After saponification of the organic extracts, extraction of the resulting fatty acids into acidified ethyl ether, and evaporation under N_2, residues were dissolved in MeOH for mass spectrometric analysis.

Microsomal CYP-mediated EET Biosynthesis

CYP Supersomes™ (Corning, NY) (60 nM, final concentration) were incubated at 37 °C for 30 min in the presence of AA (120 μM) in 0.5 ml potassium phosphate buffer, (50 mM, pH 7.4), containing 1 mM EDTA and 1 mM NADPH. Reactions were terminated by adding methylene chloride (0.5 ml). Samples were centrifuged at 3,000 rpm for 10 minutes and 150 μl of the organic phase was aspirated and evaporated to dryness under a gentle stream of nitrogen gas. Residues were then reconstituted in 20 μl of MeOH containing [^{13}C-20]EET internal standard and resultant samples were analyzed by mass spectrometry.

Quantification and Statistical Analysis

Statistical parameters and statistical significance are reported in the Figures and Figure Legends. Data is reported to be statistically significant when $p < 0.05$ by Student's t test.

Supplementary Material

Refer to Web version on PubMed Central for supplementary material.

Acknowledgments

R01-CA113570, Susan G. Komen Foundation grant KG090861, Randy Shaver Foundation and Community Fund, Minnesota Partnership for Biotechnology and Medical Genomics, University of Minnesota (UMN) Medical School Research Renewal Program to D.A.P. and Dr. Carol Lange, the Fairview Foundation Dr. Barbara Bowers Fund, and the State of Minnesota through the Translational Product Development Fund (TPDF with R.J.S.) to D.A.P. The Walther Prize for Cancer Research to D.G.T and D.A.P. We also acknowledge Masonic Cancer Center NIH grant P30-CA077598 (Dr. Douglas Yee, P.I.) for Analytical Biochemistry core support and the National Center for Advancing Translational Sciences of the NIH Award Numbers UL1TR000114 and UL1TR000135 (Dr. Bruce Blazar, P.I.). Instituto Nacional de Cancerologica de Mexico, Patronato del Instituto Nacional de Cancerologia, Consejo Nacional de Ciencia y Tecnologia, grant 280148 for visiting student support. Support is acknowledged of grants R01 ES025767 to I.F.S., R01 GM57353 to T.L.P. and NIH MIRA award R35 GM118145 to S.G.S., NIH MIRA R35 GM118030 to J.D.L, R01 CA157971 to A.K., F31 CA177119 to E.A.H., NIH GM110790 to W.M.A., P30ES013508 to I.A.B. and P30CA016520 (Dr. Chi Dang, P.I.), 5R01-GM037922 and 5P01-DK038226 to J.H.C., and NIH U01 HL117664 to K.G. Students Juan Alvarez and William Marrero Ortiz were supported by LSSURP grant R25 HL088728 to Dr. Colin Campbell. The content is solely the responsibility of the authors and does not necessarily represent the official views of the NIH. E.A. acknowledges support of UMN Department of Medicinal Chemistry and the UMN Supercomputing Institute for Advanced Computational Research (MSI). Support is acknowledged of Fashion Footwear Charitable Foundation of New York/QVC Presents Shoes on Sale™ (to D.G.T.) and the National Research Fund of Korea grant 2015R15A2009124 (to Y.K.B.). Support is acknowledged of the Robert A. Welch Foundation (I-0011) and the Dr. Ralph and Marian Falk Medical Research Trust to J.R.F. Support is acknowledged of the Center for Translational Medicine of the UMN. We acknowledge gifts from patients and their families and Epsilon Sigma Alpha Foundation, Beta Sigma Chapter to the UMN Foundation and Minnesota International Medicine. We thank Drs. Carol Lange, Douglas Yee, Bruce Hammock, Martin Brand, Chi Dang, Phillip A. Sharp, Jeffrey Miller, Margot Cleary, Deepali Sachdev, Tom Makris, Matthew Vander Heiden, Henry Wong, Peter Villalta, Jeffry P. Jones, Ranjana Mitra, and David Donner for helpful discussions and Drs. Daniel Weisdorf, Philip McGlave, Peter Igarashi, Tucker LeBien and Bruce Blazar for their support. We thank Robin Bliss, Lia Coicou, Natalie Pascutoi, William Marrero Ortiz, Monique Morgan, Michael Maher, Christian Torres, Diego Hinojosa, Julia Nguyen and Dr. Kathryn J. Chavez for expert assistance. We thank Dr. Stephen C. Schmechel, Jonathan Henriksen and Colleen Forster for pathology core laboratory support. We thank Drs. Christophe Morisseau and Sung Hee Hwang for t-AUCB and Dr. John Imig for EET C22. We thank Michael Franklin for help with editing of the manuscript. Mitochondrial image credit for graphical abstract is: Extender_01/stock.adobe.com.

References

Addya S, Anandatheerthavarada HK, Biswas G, Bhagwat SV, Mullick J, Avadhani NG. Targeting of NH2-terminal-processed microsomal protein to mitochondria: a novel pathway for the biogenesis of hepatic mitochondrial P450MT2. J Cell Biol. 1997; 139:589–599. [PubMed: 9348277]

Bae YK, Gong G, Kang J, Lee A, Cho EY, Lee JS, Suh KS, Lee DW. Hormone receptor expression in invasive breast cancer among Korean women and comparison of 3 antiestrogen receptor antibodies: a multi-institutional retrospective study using tissue microarrays. Am J Surg Pathol. 2012; 36:1817–1825. [PubMed: 23154769]

Batchu SN, Lee SB, Samokhvalov V, Chaudhary KR, El-Sikhry H, Weldon SM, Seubert JM. Novel soluble epoxide hydrolase inhibitor protects mitochondrial function following stress. Can J Physiol Pharmacol. 2012; 90:811–823. [PubMed: 22624559]

Chandel NS, Avizonis D, Reczek CR, Weinberg SE, Menz S, Neuhaus R, Christian S, Haegebarth A, Algire C, Pollak M. Are Metformin Doses Used in Murine Cancer Models Clinically Relevant? Cell Metab. 2016; 23:569–570. [PubMed: 27076070]

Chen JK, Capdevila J, Harris RC. Cytochrome p450 epoxygenase metabolism of arachidonic acid inhibits apoptosis. Mol Cell Biol. 2001; 21:6322–6331. [PubMed: 11509673]

Choi J, Lee JH, Koh I, Shim JK, Park J, Jeon JY, Yun M, Kim SH, Yook JI, Kim EH, et al. Inhibiting stemness and invasive properties of glioblastoma tumorsphere by combined treatment with temozolomide and a newly designed biguanide (HL156A). Oncotarget. 2016; 7:65643–65659. [PubMed: 27582539]

Choi YH, Lee MG. Pharmacokinetic and pharmacodynamic interaction between nifedipine and metformin in rats: competitive inhibition for metabolism of nifedipine and metformin by each other via CYP isozymes. Xenobiotica. 2012; 42:483–495. [PubMed: 22416982]

Deng XS, Wang S, Deng A, Liu B, Edgerton SM, Lind SE, Wahdan-Alaswad R, Thor AD. Metformin targets Stat3 to inhibit cell growth and induce apoptosis in triple-negative breast cancers. Cell Cycle. 2012; 11:367–376. [PubMed: 22189713]

Denisov IG, Baas BJ, Grinkova YV, Sligar SG. Cooperativity in cytochrome P450 3A4: linkages in substrate binding, spin state, uncoupling, and product formation. J Biol Chem. 2007; 282:7066–7076. [PubMed: 17213193]

Dowling RJ, Zakikhani M, Fantus IG, Pollak M, Sonenberg N. Metformin inhibits mammalian target of rapamycin-dependent translation initiation in breast cancer cells. Cancer Res. 2007; 67:10804–10812. [PubMed: 18006825]

El-Mir MY, Nogueira V, Fontaine E, Averet N, Rigoulet M, Leverve X. Dimethylbiguanide inhibits cell respiration via an indirect effect targeted on the respiratory chain complex I. J Biol Chem. 2000; 275:223–228. [PubMed: 10617608]

El-Sikhry HE, Alsaleh N, Dakarapu R, Falck JR, Seubert JM. Novel Roles of Epoxyeicosanoids in Regulating Cardiac Mitochondria. PLoS One. 2016; 11:e0160380. [PubMed: 27494529]

Falck JR, Koduru SR, Mohapatra S, Manne R, Atcha KR, Atcha R, Manthati VL, Capdevila JH, Christian S, Imig JD, et al. 14,15-Epoxyeicosa-5,8,11-trienoic Acid (14,15-EET) surrogates: carboxylate modifications. J Med Chem. 2014; 57:6965–6972. [PubMed: 25119815]

Floriano-Sanchez E, Rodriguez NC, Bandala C, Coballase-Urrutia E, Lopez-Cruz J. CYP3A4 expression in breast cancer and its association with risk factors in Mexican women. Asian Pac J Cancer Prev. 2014; 15:3805–3809. [PubMed: 24870798]

Grinkova YV, Denisov IG, Sligar SG. Functional reconstitution of monomeric CYP3A4 with multiple cytochrome P450 reductase molecules in Nanodiscs. Biochem Biophys Res Commun. 2010; 398:194–198. [PubMed: 20599740]

Hwang SH, Morisseau C, Do Z, Hammock BD. Solid-phase combinatorial approach for the optimization of soluble epoxide hydrolase inhibitors. Bioorg Med Chem Lett. 2006; 16:5773–5777. [PubMed: 16949285]

Iliopoulos D, Hirsch HA, Struhl K. Metformin decreases the dose of chemotherapy for prolonging tumor remission in mouse xenografts involving multiple cancer cell types. Cancer Res. 2011; 71:3196–3201. [PubMed: 21415163]

Jain AN. Surflex-Dock 2.1: robust performance from ligand energetic modeling, ring flexibility, and knowledge-based search. J Comput Aided Mol Des. 2007; 21:281–306. [PubMed: 17387436]

Jiang JG, Chen CL, Card JW, Yang S, Chen JX, Fu XN, Ning YG, Xiao X, Zeldin DC, Wang DW. Cytochrome P450 2J2 promotes the neoplastic phenotype of carcinoma cells and is up-regulated in human tumors. Cancer Res. 2005; 65:4707–4715. [PubMed: 15930289]

Jiang JG, Ning YG, Chen C, Ma D, Liu ZJ, Yang S, Zhou J, Xiao X, Zhang XA, Edin ML, et al. Cytochrome p450 epoxygenase promotes human cancer metastasis. Cancer Res. 2007; 67:6665–6674. [PubMed: 17638876]

Kallinowski F, Schlenger KH, Runkel S, Kloes M, Stohrer M, Okunieff P, Vaupel P. Blood flow, metabolism, cellular microenvironment, and growth rate of human tumor xenografts. Cancer Res. 1989; 49:3759–3764. [PubMed: 2736517]

Kapucuoglu N, Coban T, Raunio H, Pelkonen O, Edwards RJ, Boobis AR, Iscan M. Expression of CYP3A4 in human breast tumour and non-tumour tissues. Cancer Lett. 2003; 202:17–23. [PubMed: 14643022]

Katragadda D, Batchu SN, Cho WJ, Chaudhary KR, Falck JR, Seubert JM. Epoxyeicosatrienoic acids limit damage to mitochondrial function following stress in cardiac cells. J Mol Cell Cardiol. 2009; 46:867–875. [PubMed: 19285984]

Kim A, Shin HC, Bae YK, Kim MK, Kang SH, Lee SJ, Lee EH. Multiplication of Chromosome 17 Centromere Is Associated with Prognosis in Patients with Invasive Breast Cancers Exhibiting Normal HER2 and TOP2A Status. J Breast Cancer. 2012a; 15:24–33. [PubMed: 22493625]

Kim J, Kundu M, Viollet B, Guan KL. AMPK and mTOR regulate autophagy through direct phosphorylation of Ulk1. Nat Cell Biol. 2011; 13:132–141. [PubMed: 21258367]

Kim, SW., Jun, SS., Min, CH., Kim, YW., Kang, MS., Oh, BK., Park, SH., Kim, YE., Kim, D., Lee, JS., et al. Biguanide Derivative, A Preparation Method Thereof and a Pharmaceutical Composition Containing the Biguanide Derivative as an Active Ingredient. U.S.P.a.T. Office. , editor. Korea: Hanall Biopharma Co., Ltd.; 2012b. p. 1-14.

Labitzke EM, Diani-Moore S, Rifkind AB. Mitochondrial P450-dependent arachidonic acid metabolism by TCDD-induced hepatic CYP1A5; conversion of EETs to DHETs by mitochondrial soluble epoxide hydrolase. Arch Biochem Biophys. 2007; 468:70–81. [PubMed: 17959137]

Liu B, Fan Z, Edgerton SM, Deng XS, Alimova IN, Lind SE, Thor AD. Metformin induces unique biological and molecular responses in triple negative breast cancer cells. Cell Cycle. 2009; 8:2031–2040. [PubMed: 19440038]

Luthra A, Gregory M, Grinkova YV, Denisov IG, Sligar SG. Nanodiscs in the studies of membrane-bound cytochrome P450 enzymes. Methods Mol Biol. 2013; 987:115–127. [PubMed: 23475672]

Ma J, Guo Y, Chen S, Zhong C, Xue Y, Zhang Y, Lai X, Wei Y, Yu S, Zhang J, et al. Metformin enhances tamoxifen-mediated tumor growth inhibition in ER-positive breast carcinoma. BMC Cancer. 2014; 14:172. [PubMed: 24612549]

Madiraju AK, Erion DM, Rahimi Y, Zhang XM, Braddock DT, Albright RA, Prigaro BJ, Wood JL, Bhanot S, MacDonald MJ, et al. Metformin suppresses gluconeogenesis by inhibiting mitochondrial glycerophosphate dehydrogenase. Nature. 2014; 510:542–546. [PubMed: 24847880]

Merabet N, Bellien J, Glevarec E, Nicol L, Lucas D, Remy-Jouet I, Bounoure F, Dreano Y, Wecker D, Thuillez C, et al. Soluble epoxide hydrolase inhibition improves myocardial perfusion and function in experimental heart failure. J Mol Cell Cardiol. 2012; 52:660–666. [PubMed: 22155238]

Mitra R, Guo Z, Milani M, Mesaros C, Rodriguez M, Nguyen J, Luo X, Clarke D, Lamba J, Schuetz E, et al. CYP3A4 Mediates Growth of Estrogen Receptor-positive Breast Cancer Cells in Part by Inducing Nuclear Translocation of Phospho-Stat3 through Biosynthesis of ({+/−})-14,15-Epoxyeicosatrienoic Acid (EET). J Biol Chem. 2011; 286:17543–17559. [PubMed: 21402692]

Murray GI, Patimalla S, Stewart KN, Miller ID, Heys SD. Profiling the expression of cytochrome P450 in breast cancer. Histopathology. 2010; 57:202–211. [PubMed: 20716162]

Nath A, Grinkova YV, Sligar SG, Atkins WM. Ligand binding to cytochrome P450 3A4 in phospholipid bilayer nanodiscs: the effect of model membranes. J Biol Chem. 2007; 282:28309–28320. [PubMed: 17573349]

Panigrahy D, Edin ML, Lee CR, Huang S, Bielenberg DR, Butterfield CE, Barnes CM, Mammoto A, Mammoto T, Luria A, et al. Epoxyeicosanoids stimulate multiorgan metastasis and tumor dormancy escape in mice. J Clin Invest. 2012; 122:178–191. [PubMed: 22182838]

Pozzi A, Popescu V, Yang S, Mei S, Shi M, Puolitaival SM, Caprioli RM, Capdevila JH. The anti-tumorigenic properties of peroxisomal proliferator-activated receptor alpha are arachidonic acid epoxygenase-mediated. J Biol Chem. 2010; 285:12840–12850. [PubMed: 20178979]

Row H, Jeong J, Cho S, Kim S, Kim K. HL271, a novel chemical compound derived from metformin, differs from metformin in its effects on the circadian clock and metabolism. Biochem Biophys Res Commun. 2016; 469:783–789. [PubMed: 26707879]

Samokhvalov V, Alsaleh N, El-Sikhry HE, Jamieson KL, Chen CB, Lopaschuk DG, Carter C, Light PE, Manne R, Falck JR, et al. Epoxyeicosatrienoic acids protect cardiac cells during starvation by modulating an autophagic response. Cell Death Dis. 2013; 4:e885. [PubMed: 24157879]

Shackelford DB, Abt E, Gerken L, Vasquez DS, Seki A, Leblanc M, Wei L, Fishbein MC, Czernin J, Mischel PS, et al. LKB1 inactivation dictates therapeutic response of non-small cell lung cancer to the metabolism drug phenformin. Cancer Cell. 2013; 23:143–158. [PubMed: 23352126]

Srirangam A, Mitra R, Wang M, Gorski JC, Badve S, Baldridge L, Hamilton J, Kishimoto H, Hawes J, Li L, et al. Effects of HIV protease inhibitor ritonavir on Akt-regulated cell proliferation in breast cancer. Clin Cancer Res. 2006; 12:1883–1896. [PubMed: 16551874]

Wang B, Zeng H, Wen Z, Chen C, Wang DW. CYP2J2 and its metabolites (epoxyeicosatrienoic acids) attenuate cardiac hypertrophy by activating AMPKalpha2 and enhancing nuclear translocation of Akt1. Aging Cell. 2016; 15:940–952. [PubMed: 27416746]

Wang D, Dubois RN. Epoxyeicosatrienoic acids: a double-edged sword in cardiovascular diseases and cancer. J Clin Invest. 2012; 122:19–22. [PubMed: 22182836]

Ward JP. Oxygen sensors in context. Biochim Biophys Acta. 2008; 1777:1–14. [PubMed: 18036551]

Wheaton WW, Weinberg SE, Hamanaka RB, Soberanes S, Sullivan LB, Anso E, Glasauer A, Dufour E, Mutlu GM, Budigner GS, et al. Metformin inhibits mitochondrial complex I of cancer cells to reduce tumorigenesis. Elife. 2014; 3:e02242. [PubMed: 24843020]

Zakikhani M, Dowling R, Fantus IG, Sonenberg N, Pollak M. Metformin is an AMP kinase-dependent growth inhibitor for breast cancer cells. Cancer Res. 2006; 66:10269–10273. [PubMed: 17062558]

Zeldin DC, Wei S, Falck JR, Hammock BD, Snapper JR, Capdevila JH. Metabolism of epoxyeicosatrienoic acids by cytosolic epoxide hydrolase: substrate structural determinants of asymmetric catalysis. Arch Biochem Biophys. 1995; 316:443–451. [PubMed: 7840649]

Zhang B, Zhao R, He Y, Fu X, Fu L, Zhu Z, Fu L, Dong JT. MicroRNA 100 sensitizes luminal A breast cancer cells to paclitaxel treatment in part by targeting mTOR. Oncotarget. 2016; 7:5702–5714. [PubMed: 26744318]

Zhang Y, El-Sikhry H, Chaudhary KR, Batchu SN, Shayeganpour A, Jukar TO, Bradbury JA, Graves JP, DeGraff LM, Myers P, et al. Overexpression of CYP2J2 provides protection against doxorubicin-induced cardiotoxicity. Am J Physiol Heart Circ Physiol. 2009; 297:H37–46. [PubMed: 19429816]

Highlights

- CYP3A4 is an arachidonic acid (AA) epoxygenase required for breast tumor formation.
- CYP3A4 suppresses autophagy in breast cancer, in part, by inhibiting AMPK activation.
- CYP3A4 AA epoxygenase activity promotes the mitochondrial electron transport chain.
- Metformin inhibits breast cancer by inhibiting CYP3A4 AA epoxygenase activity.

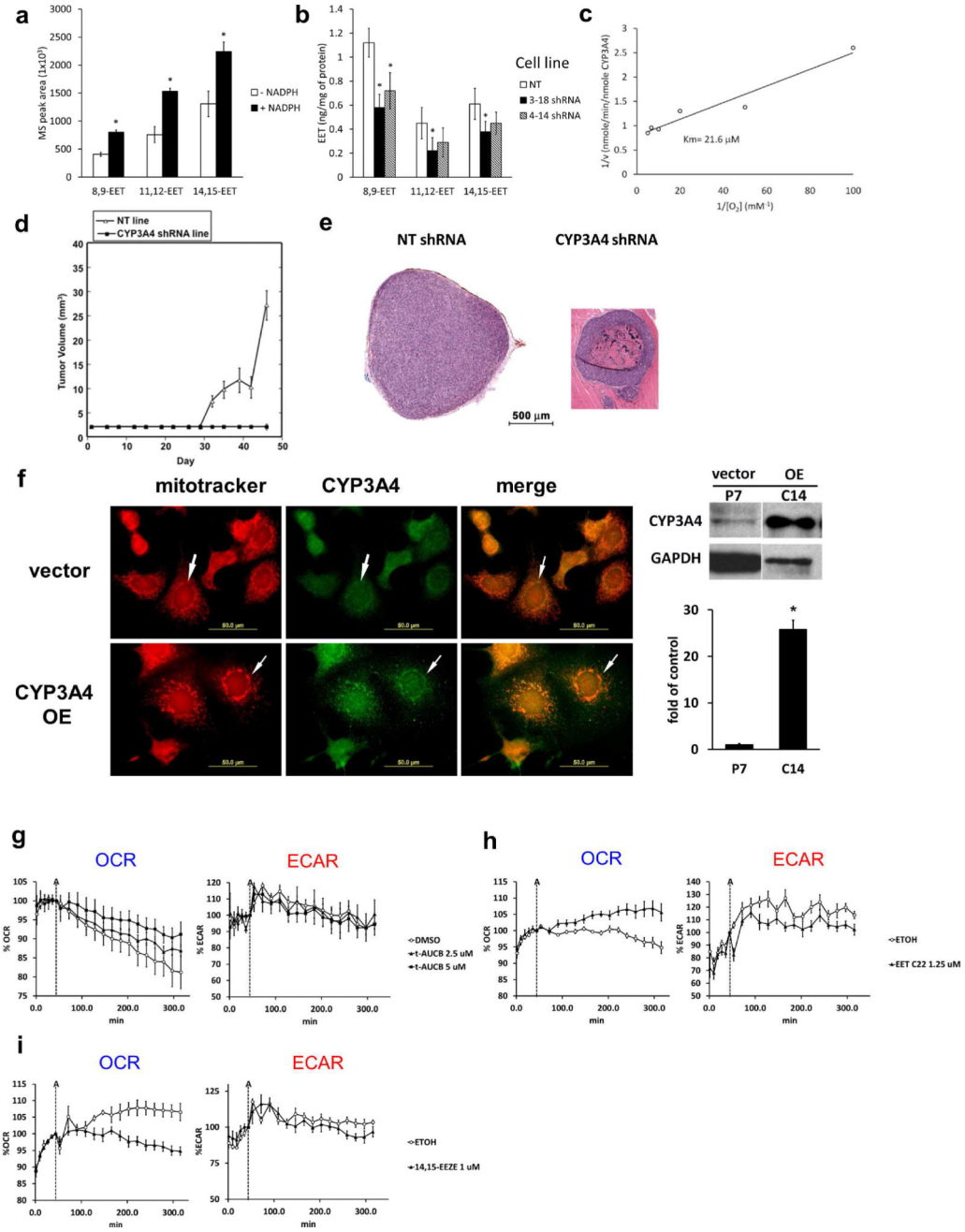

Figure 1.

Cancer cell intrinsic CYP3A4 is required for tumor growth and synthesizes EETs, which regulate mitochondrial homeostasis. **a**. CYP3A4 nanodisc-mediated synthesis of EETs from AA is NADPH-dependent. Results are expressed as mean of peak area ± S.D. (n=3, * indicates P<0.05). **b**. Cellular EET regioisomer levels in MCF-7 CYP3A4 knockdown cell lines 3–18 and 4–14 compared to the NT2 (non-target shRNA) control cell line. Results are expressed as mean of EET regioisomer/total protein ± S.D. (n=3, * P<0.05). **c**. Lineweaver-Burk plot used to determine the K_m of O_2 for CYP3A4 catalyzed epoxidation of AA. **d**. Growth of the NT2 cell line (△) or the 3–18 CYP3A4 knockdown cell line (■) in the

mammary fat pad of nude mice (Gompertzian curve fitting; P = 0.0101 for difference between the two growth curves). **e**. CYP3A4 knockdown tumors (3–18 cell line; right) exhibited central necrosis while control cell-line derived tumors (NT2 cell line; left) lacked necrosis (p=0.0152; two tailed Fisher's exact test for presence of necrosis in the knockdown tumors). Size bar is 500 μm for both images. **f**. Left panel: Co-localization of CYP3A4 and mitochondria, with or without CYP3A4 over-expression. Cells were incubated with a polyclonal antibody to CYP3A4 (fluorescein secondary antibody in green) and MitoTracker Red© (red). Arrows indicate peri-nuclear structures that co-stain with MitoTracker-Red and the CYP3A4 antibody. CYP3A4 over-expressing clone C14 and control empty vector clone P7 are shown (Size bar=50 μm). Control images without primary antibody showed no fluorescence (not shown). Right panel: CYP3A4 over-expressing clone C14 expressed 25-fold higher CYP3A4 compared to empty vector (pcDNA3.1) control cell line P7 ($P=3.5\times10^{-5}$). **g**. MCF-7 cells treated with sEH inhibitor t-AUCB or DMSO vehicle beginning at time point "A" and subsequently assayed for OCR (left panel) and ECAR (right panel). OCR was significantly increased at the endpoint by t-AUCB in a concentration dependent fashion (t test at end point of 2.5 μM t-AUCB vs. DMSO vehicle P=0.024; 5 μM P=0.0033). **h.** Effect of EET analog EET C22 on OCR (left panel; end point P=0.019) and ECAR (right panel; end point P=0.034). **i.** EET antagonist 14,15-EEZE (1.0 μM) added at time point "A" suppressed OCR (left panel) and ECAR (right panel) (end point p-values: %OCR 0.003; %ECAR 0.0055).

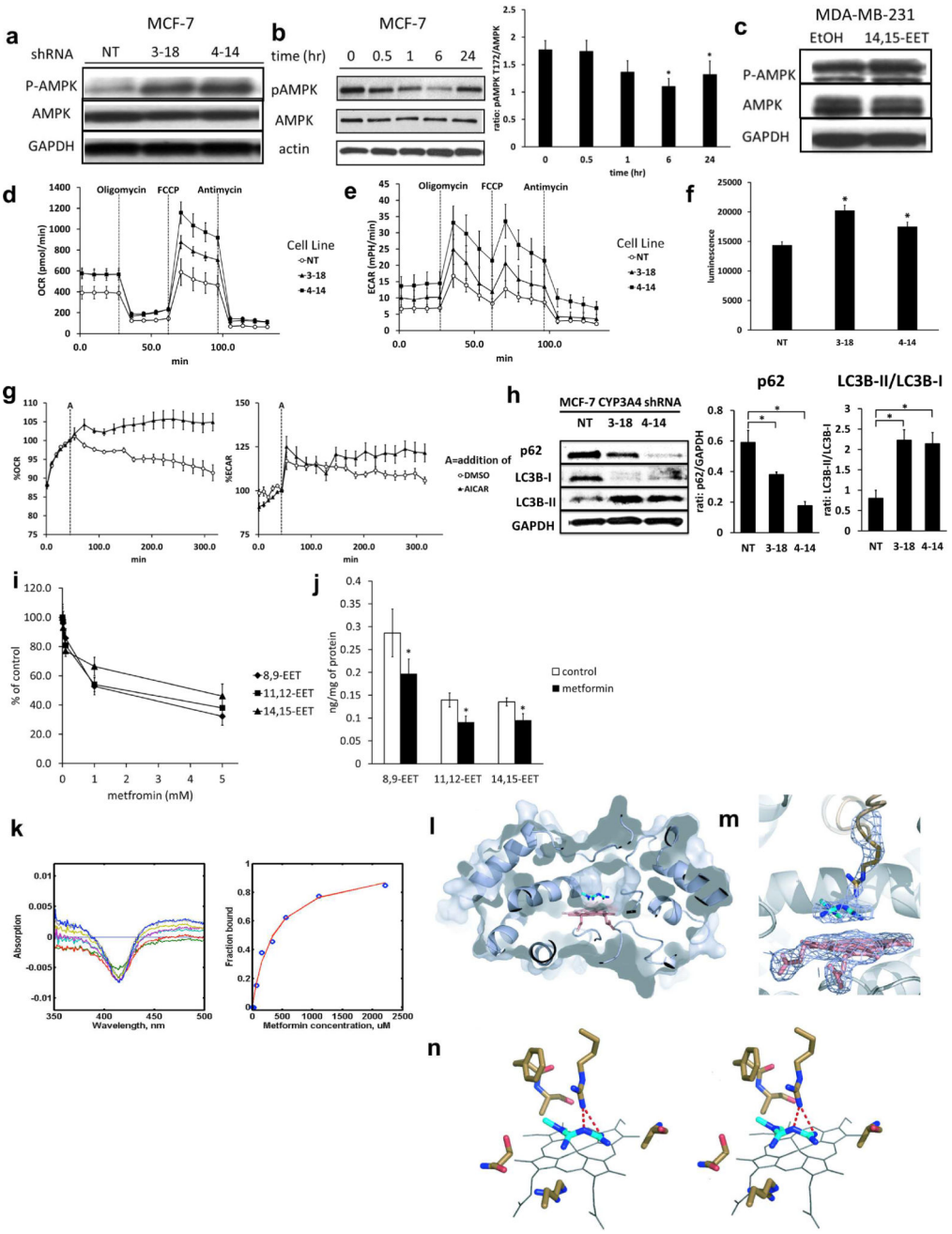

Figure 2.

CYP3A4 suppresses AMPK through its EET products, while metformin binds to the CYP3A4 active site heme and inhibits EET biosynthesis. **a**. AMPKα phosphorylation (p-Thr172) was increased in MCF-7 CYP3A4 knockdown (shRNA) clones 3–18 and 4–14 vs. the NT2 (non-target) control line (n=3, P<0.05). **b**. AMPKα phosphorylation was decreased in MCF-7 cells after exposure to (±)-14,15-EET (1 μM) (P<0.05 for the 6 and 24 hour time points). **c**. AMPKα phosphorylation in MDA-MB-231 cells was unaffected by exposure to (±)-14,15-EET (1 μM) for 24 hours. **d.** CYP3A4 knockdown in MCF-7 cells resulted in increased basal OCR and spare respiratory capacity, as well as increased OCR after FCCP

treatment. (10^5 cells per well, n=6) **e.** CYP3A4 knockdown increased basal ECAR, which was further increased with inhibition by oligomycin and FCCP, suggesting transient catabolic compensation for loss of mitochondrial function (10^5 cells per well, n=6). **f.** MCF-7 CYP3A4 knockdown cell lines exhibited higher cellular ATP levels than control. Results are represented as mean ± S.D. (n=3, * indicates $p < 0.05$ vs. control). **g.** AICAR (100 μM) activated OCR (left panel) and ECAR (right panel) in MCF-7 cells. End point P-values: %OCR 0.0026; %ECAR 0.047. **h.** The autophagy marker p62 was depleted and the LC3B-II/LCB-I ratio was increased in the CYP3A4 knockdown cell lines (* indicates $P<0.05$). **i.** Inhibition of microsomal CYP3A4-mediated biosynthesis of (±)-8,9-, 11,12-, and 14,15-EET after 30 minutes exposure to the indicated concentrations of metformin. **j**. Cellular EET regioisomers measured in MCF-7 cells exposed to 5 mM metformin or vehicle for 6 hours, normalized to cellular protein. (*, n=3, $P<0.05$). **k**. Left panel. Type I spin shift induced by metformin interaction with CYP3A4 nanodiscs, shown by a difference spectrum comparing heme absorbance with and without metformin. Right panel. Determination of the spectral dissociation constant (K_s ~400 μM) of metformin bound to CYP3A4 nanodiscs. The red line is a fitted curve. **l**. Metformin co-crystalized with CYP3A4 in the active site near the heme (**m**). **n.** Metformin forms a hydrogen bond with R212 in the F-F' loop of CYP3A4 (stereo view).

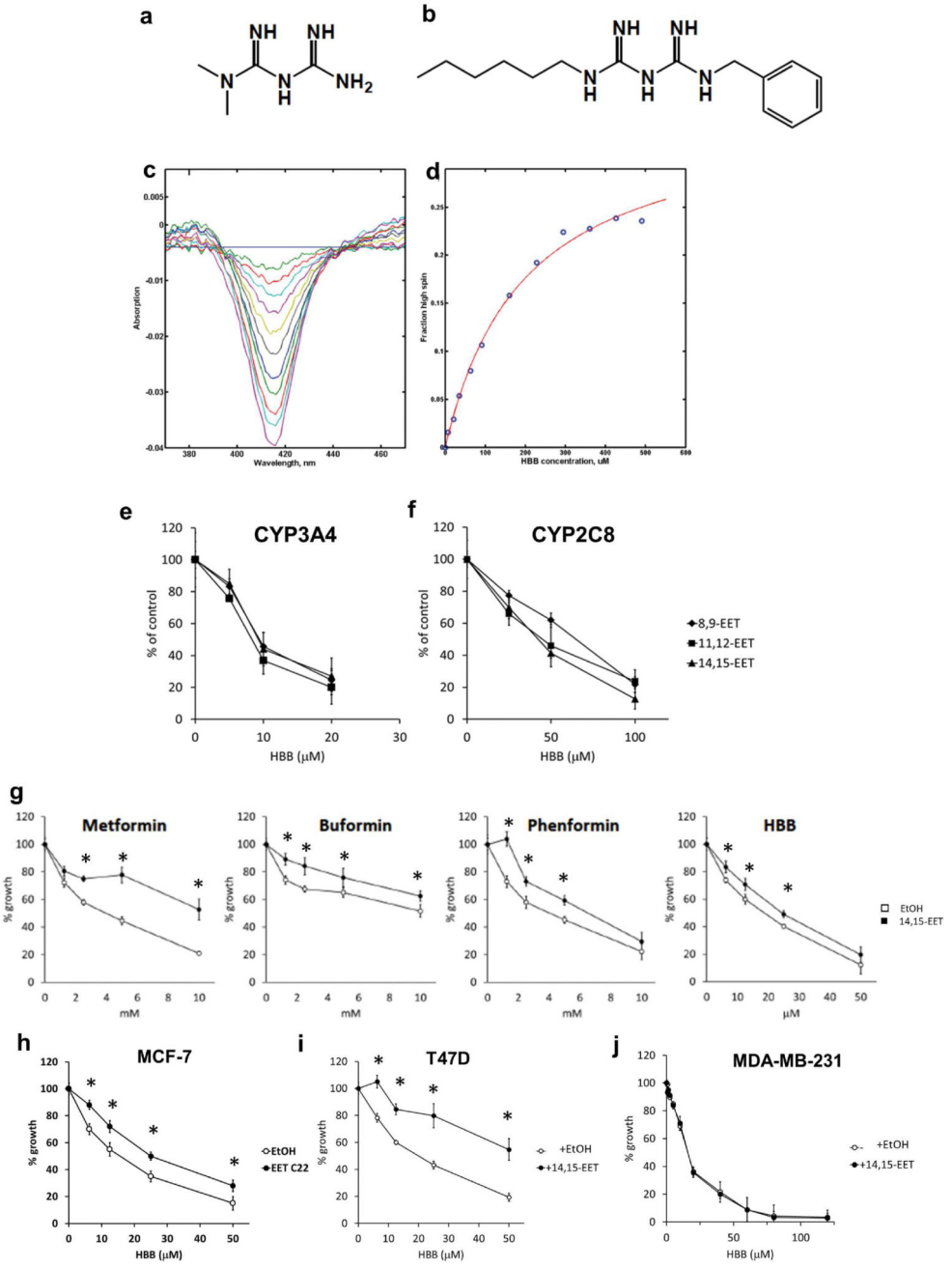

Figure 3.

N1-hexyl-N5-benzyl-biguanide (HBB) potently inhibited MCF-7 cell proliferation, in part, through inhibition of CYP3A4 AA epoxygenase activity. **a.** Metformin structure. **b.** HBB structure. **c**. Type I spin shift induced by HBB interaction with CYP3A4 nanodiscs. **d**. Determination of the spectral dissociation constant of HBB bound to CYP3A4 nanodiscs (K_s ~110 μM). The red line is a fitted curve. **e**. Microsomal CYP3A4-mediated biosynthesis of EET regioisomers after 30 minutes exposure to the indicated concentrations of HBB. **f**. Microsomal CYP2C8-mediated biosynthesis of EETs after 30 minutes exposure to the indicated concentrations of HBB. **g**. MCF-7 cell growth after treatment with metformin,

buformin, phenformin, or HBB at the indicated concentrations in the presence or absence of concurrent treatment with (±)-14,15-EET (1 μM). Cell growth was measured by MTT assay at 24 hours after addition of biguanide or vehicle (PBS vehicle for metformin, DMSO for the other biguanides) and (±)-14,15-EET (1 μM) or vehicle (ethanol). Results are expressed as percent growth relative to control, mean ± S.E.M, n=8. (* $P<0.05$). **h.** EET C22 partially abrogated HBB-mediated growth inhibition of the MCF-7 cell line (* $P<0.05$). **i.** (±)-14,15-EET largely abrogated HBB-mediated growth inhibition of the T47D cell line (* $P<0.05$). **j.** (±)-14,15-EET failed to affect HBB-mediated growth inhibition of the MDA-MB-231 cell line. Similar results were found for the MDA-MB-435/LCC6 cell line (data not shown).

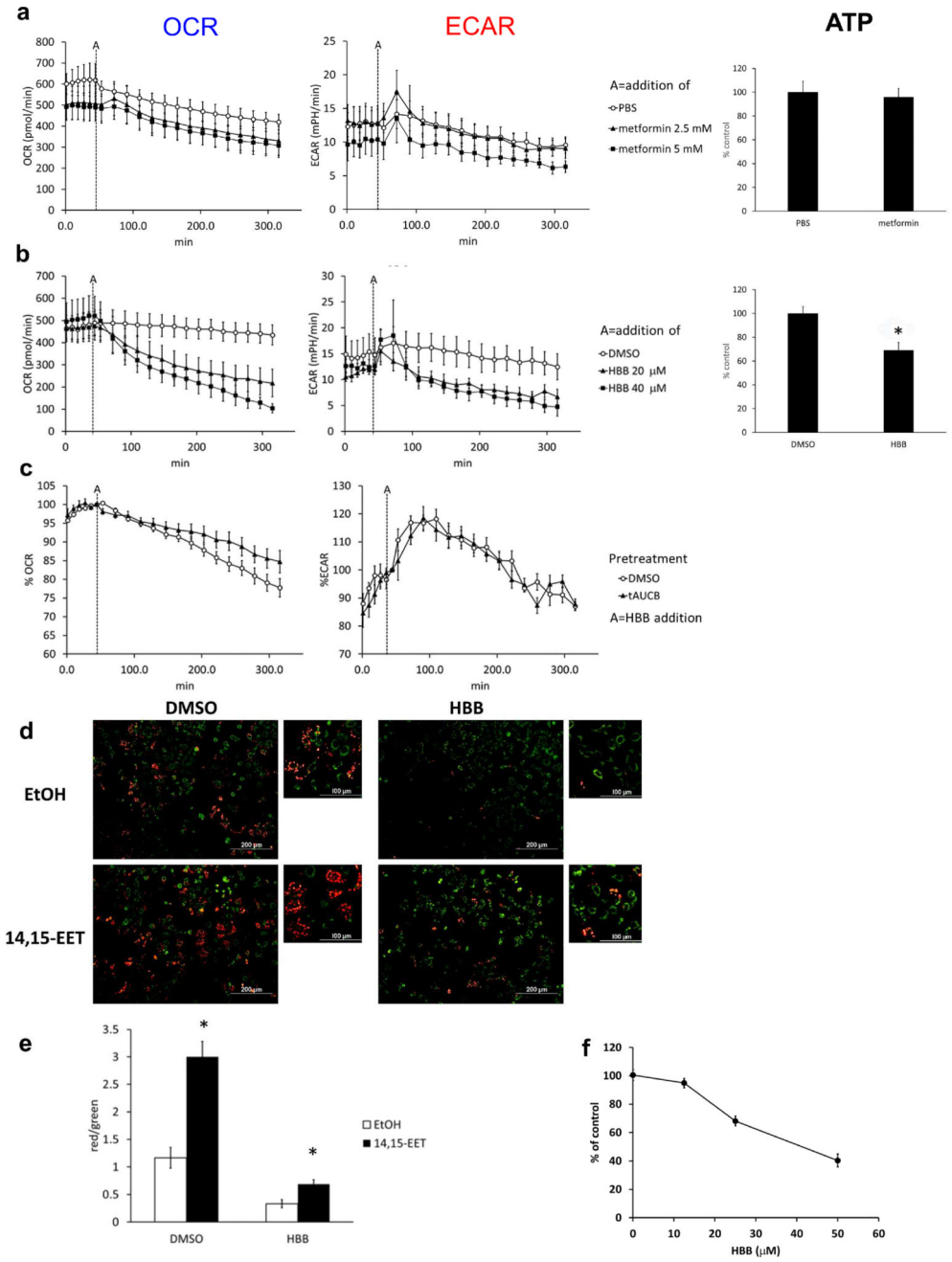

Figure 4.

HBB inhibits OCR and ECAR in MCF-7 cells and suppresses the ETC, in part, through reduction of (±)-14,15-EET. **a**. OCR and ECAR after treatment with metformin (2.5 and 5 mM) or PBS control were not significantly different (by Student t test) after 270 minutes of treatment. (10^5 cells per well). Total cellular ATP levels were unchanged after 6 hours of metformin treatment (right panel). Biguanide was added at time "A" in a, b and c. **b**. OCR and ECAR were reduced by HBB and the reduction was significant at the endpoint of A +270 minutes. The HBB OCR endpoints were less than the DMSO endpoint (20 μM P= 0.0014; 40 μM $P=2.5\times10^{-5}$) (left panel). The HBB ECAR endpoints were less than the

DMSO endpoint (20 μM P= 0.0021; 40 μM P=0.00050 by t test) (middle panel). Total cellular ATP levels were reduced at 6 hours of HBB treatment (P<0.05 by t test; right panel). **c**. Pre-treatment with t-AUCB (5 μM) vs. DMSO control partially protected OCR, but not ECAR, from HBB-mediated inhibition. t-AUCB or DMSO was added before addition of HBB (20 μM) at time A (A-120 minutes). OCR at the endpoint was higher for t-AUCB (5 μM) pretreatment (P=0.00011, by t test), but ECAR at the endpoint was not (P=0.33, by t test)(mean ± S.D; n=5). **d**. ΔΨm, visualized by JC-1 dye staining, was reduced by HBB in MCF-7 cells and partially restored by (±)-14,15-EET. Representative images are shown, with higher magnification in insets. Compared to control (upper left panel), HBB (20 μM) treatment for 4 hours caused mitochondrial depolarization in MCF-7 cells (upper right panel) and (±)-14,15-EET (1 μM) provided partial protection (bottom right panel); (±)-14,15-EET (1 μM) alone increased mitochondrial cross membrane potential (bottom left panel) relative to control. Size bar 200 μm and for insets 100 μm. **e**. The red/green ratios in experiments shown in **d.** were quantified and presented as mean ± S.D (n=4) (* indicates P<0.05). **f.** TMRE measurement of HBB effect on ΔΨm in MCF-7 cells. TMRE was used to measure ΔΨm under non-quenching conditions (500 nM concentration) (Fig.S5c,d).

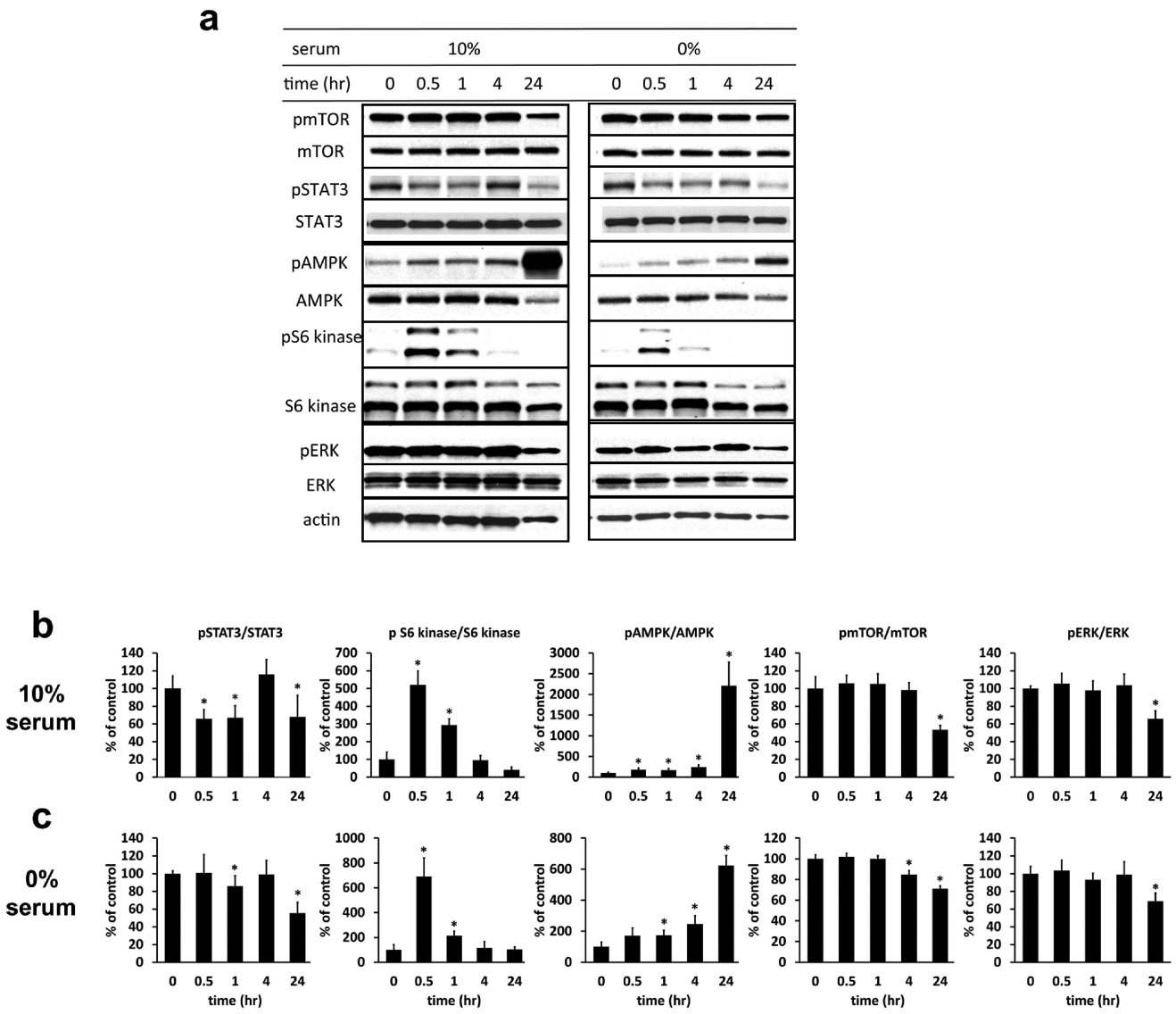

Figure 5.

HBB results in early and progressive AMPKα activation, transient early activation of p70 S6 Kinase, and later mTOR and ERK1/2 inhibition, in the presence or absence of serum. **a.** Western blot time course of signaling proteins of MCF-7 cells grown in complete media (10 % serum) or serum starved (~16 hours) and treated with HBB (20 μM). Phosphorylation sites studied were AMPKα-Thr172; p70 S6 Kinase-Thr389; mTOR-Ser2448; ERK1/2 (p44/42 MAPK)-Thr202/Tyr204 and STAT3-Tyr705. **b–c**. Quantification of the western blotting analysis in **a.** (**b.** 10% serum, **c.** serum starvation; n=3, * indicates $p < 0.05$).

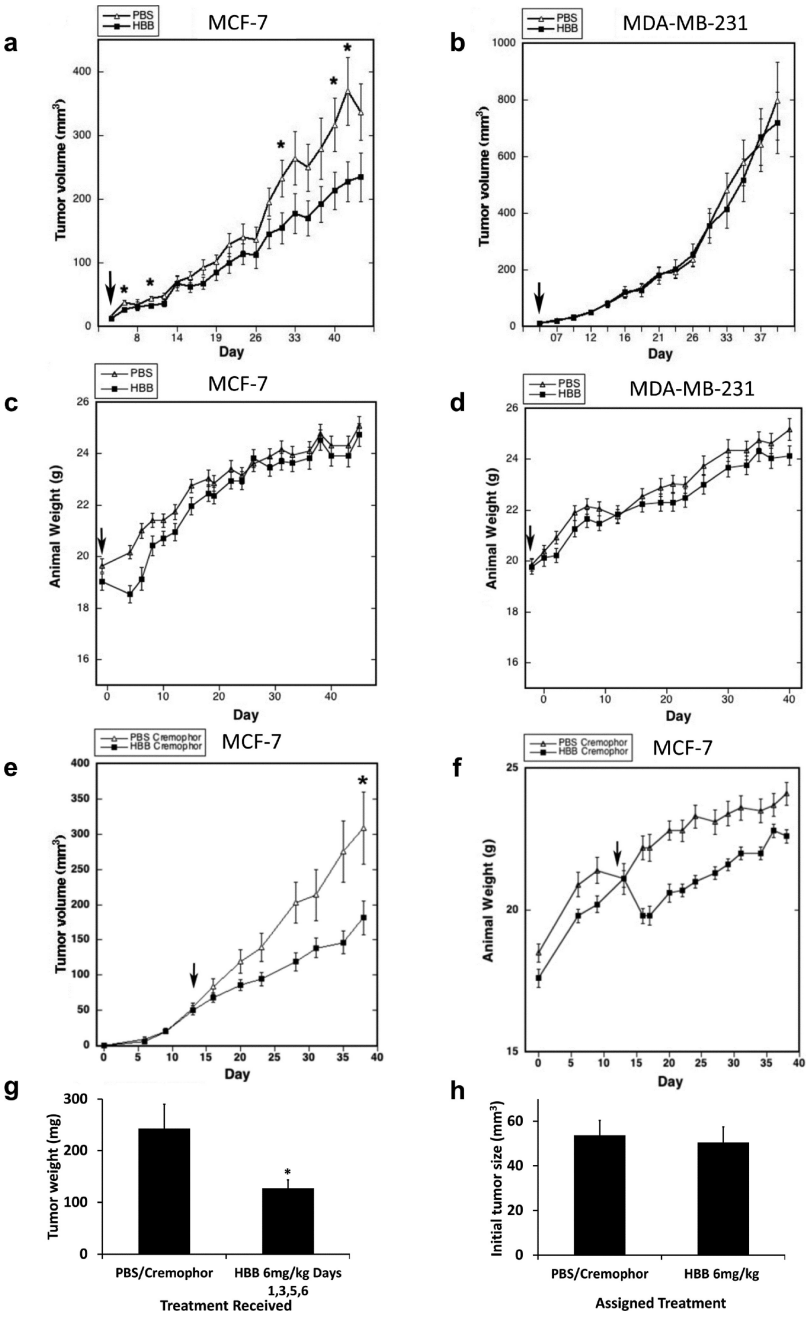

Figure 6.

HBB inhibited the MCF-7, but not the MDA-MB-231 mammary fat pad xenograft. At the minimal effective dose (MED), HBB inhibited MCF-7, but not MDA-MB-231 tumor growth and at higher dosing the MCF-7 xenograft model exhibited greater inhibition. **a.** MCF-7 mammary fat pad xenograft model with estradiol stimulation. Arrow indicates the time of treatment initiation, the day after implantation, with HBB at 4 mg/kg/day or PBS (n=20 mice per group). Tumor size in the HBB group was smaller at indicated times (* by t test), and by Gompertizan fitting the tumor growth curves (Srirangam et al., 2006) tumors of the HBB treated mice were smaller than the vehicle-treated from day 8 onward (P= 0.0354). **b.**

Triple negative MDA-MB-231 mammary fat pad xenograft model treated with HBB or PBS. Arrow indicates the time of treatment initiation, the day after implantation, with HBB at 4 mg/kg/day or PBS (n=20 mice per group). Tumor size in the HBB-treated group was indistinguishable from the vehicle-treated group. **c.** Weights of mice bearing MCF-7 tumors treated with either HBB or PBS. **d.** Weights of mice bearing MDA-MB-231 tumors treated with either HBB or PBS. **e.** MCF-7 mammary fat pad xenograft model with estradiol stimulation treated with HBB at the MTD vs. vehicle. Arrow indicates the time of treatment initiation when tumors averaged 50 mm^3 (n=15 mice per group). Daily treatment (6 mg/kg ip) was given for the first three days, followed by weight loss. The treatment schedule was then changed to 4 days of 7 with no more than 2 consecutive days of dosing, repeating each week. Tumor size in the HBB group was smaller at the endpoint of treatment (*; P= 0.039). **f.** Weights of mice treated with either vehicle or HBB. Arrow indicates the time of treatment initiation. Maximum weight differential of 11% on day 16 recovered to 6% by day 38. **g.** Tumor weights were lower in the HBB treated mice at the endpoint of the xenograft study in e. (*; P=0.034). **h.** Tumor sizes the day before treatment were balanced between the 2 groups. Legend for all: (△) vehicle and (■) HBB.

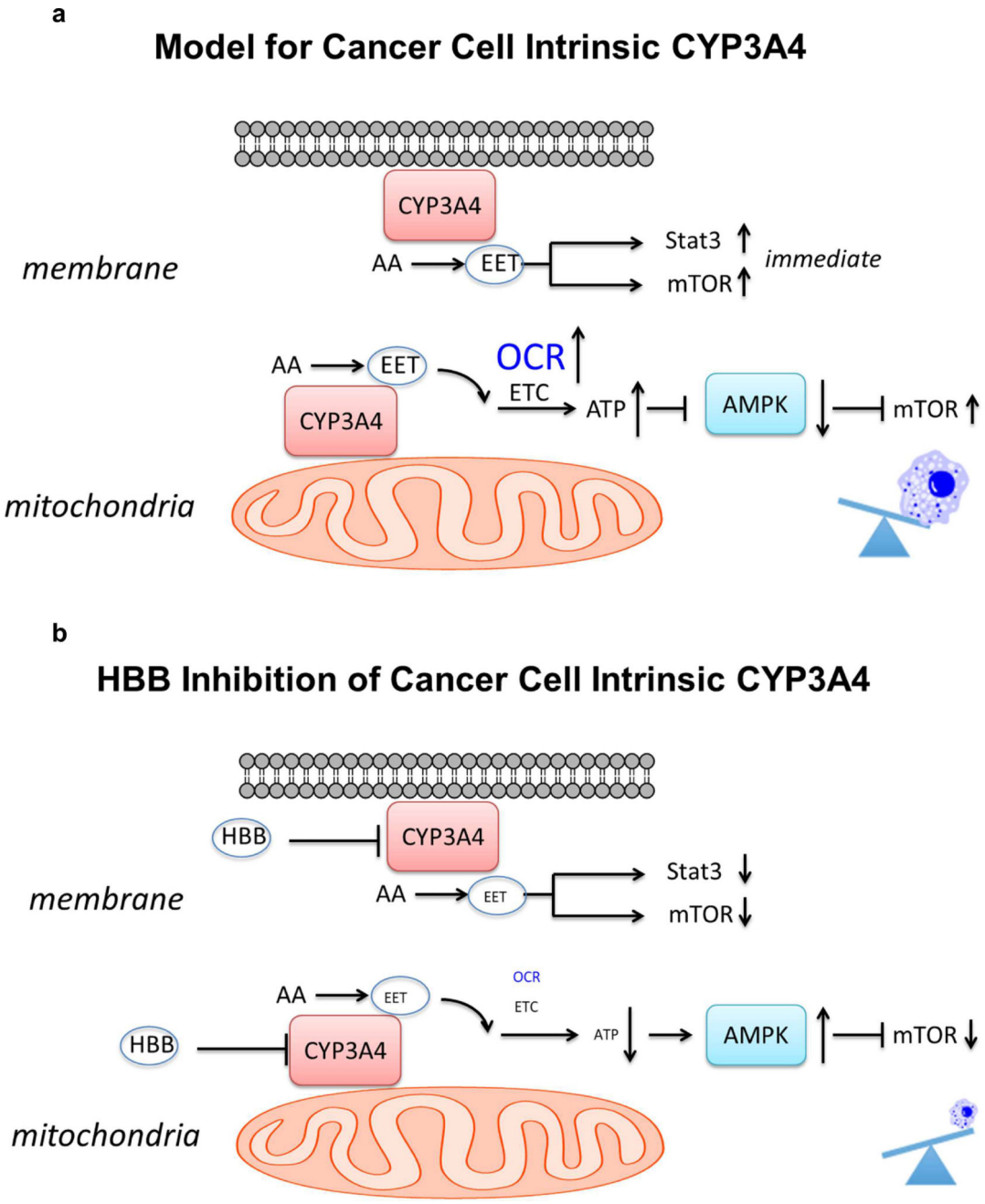

Figure 7.

CYP3A4 regulates ER+HER2− breast cancer cell growth through plasma membrane and mitochondrial mechanisms. **a.** Model for cancer cell intrinsic CYP3A4 AA epoxygenase activity. CYP3A4 synthesizes and supports basal levels of EETs (Fig.1a,b), facilitating Stat3 and mTOR signaling (Fig.5) and suppressing autophagy (Fig.2h). Mitochondrial CYP3A4 AA epoxygenase activity supports the ETC and acts as a modulator of ETC/OCR (Fig. 1g,h,i). Basal ATP levels suppress AMPK and permit mTOR activity (Fig.5), supporting biomass accumulation. Endogenous EETs promote activation of Stat3 and mTOR. Exogenous EET C22 analog (not shown) also activates OCR and suppresses ECAR (Fig.1h).

In this model, EET mediated mTOR activation promotes anabolism, shown by cartoon of increased cell mass. **b.** Model for HBB inhibition of cancer cell intrinsic CYP3A4 AA epoxygenase activity. HBB inhibits CYP3A4-mediated EET biosynthesis (Fig.3e), reducing Stat3 and mTOR signaling (Fig.5). HBB acutely inhibits mitochondrial CYP3A4 activity and OCR (Fig.4b, left panel; Fig.S3d,e,f, left panels), also resulting in suppression of ECAR (Fig.4b, middle panel; Fig.S3d,e,f, right panels) and reduction of ATP (Fig.4b right panel). We propose that depletion of ATP by HBB may inhibit priming of glycolysis. HBB-mediated ATP reduction activates AMPK (Fig.5). Exogenous (±)-14,15-EET partially restores ΔΨm/ETC in presence of HBB (Fig.4d,e and Fig.S4a,b), indicating a central role for EETs in maintaining mitochondrial function in cancer cells. In this model, HBB inhibits EET biosynthesis and mTOR, thereby reducing biomass, shown by cartoon.